Published in final edited form as:
Psychol Rev. 2013 October ; 120(4): . doi:10.1037/a0034192.

Sensory Optimization by Stochastic Tuning

Peter Jurica,
RIKEN Brain Science Institute, Wako-shi, Saitama, Japan

Sergei Gepshtein,
The Salk Institute for Biological Studies, La Jolla, California, USA

Ivan Tyukin, and
University of Leicester, Leicester, UK

Cees van Leeuwen
University of Leuven, Leuven, Belgium

Abstract

Individually, visual neurons are each selective for several aspects of stimulation, such as stimulus location, frequency content, and speed. Collectively, the neurons implement the visual system's preferential sensitivity to some stimuli over others, manifested in behavioral sensitivity functions. We ask how the individual neurons are coordinated to optimize visual sensitivity. We model synaptic plasticity in a generic neural circuit, and find that stochastic changes in strengths of synaptic connections entail fluctuations in parameters of neural receptive fields. The fluctuations correlate with uncertainty of sensory measurement in individual neurons: the higher the uncertainty the larger the amplitude of fluctuation. We show that this simple relationship is sufficient for the stochastic fluctuations to steer sensitivities of neurons toward a characteristic distribution, from which follows a sensitivity function observed in human psychophysics, and which is predicted by a theory of optimal allocation of receptive fields. The optimal allocation arises in our simulations without supervision or feedback about system performance and independently of coupling between neurons, making the system highly adaptive and sensitive to prevailing stimulation.

Keywords

visual perception; stochastic optimization; uncertainty principle; synaptic plasticity

---

Visual systems obtain sensory information using large populations of specialized neurons. Each neuron is characterized by its receptive field: a spatiotemporal window in which signals are accumulated before the neuron responds. Signals are weighted differently in different parts of receptive fields. The weighting determines the selectivity ("tuning") of the neuron to a particular pattern of stimulation. Motion-sensitive neurons, for instance, are each selective to a range of stimulus speeds within their receptive fields (Nakayama, 1985; Watson & Ahumada, 1985; Rodman & Albright, 1987).

Since the total number of neurons is limited, visual systems face a problem of resource allocation: to which stimuli they should be most sensitive. This problem is dynamic because limited neural resources are available for use in a highly variable environment. Little is known about how the resource allocation problem is solved. Do visual systems monitor which aspects of stimulation prevail in the current environment? Do they use a specialized mechanism that coordinates the allocation of receptive fields?

We propose that effective resource allocation can be understood in terms of two basic features of biological motion sensing. First is the plasticity of neuronal circuits that control the selectivity of receptive fields. It is known from studies of visual attention and adaptation that neuronal receptive field are highly variable (Barlow, 1969; Moran & Desimone, 1985; de Ruyter van Steveninck et al., 1994; Seung, 2003; Krekelberg et al., 2006; Vislay-Meltzer et al., 2006; Hietanen et al., 2007; Womelsdorf et al., 2008). This variability has a stochastic component. Even though the selectivity of individual neurons may appear stable when measured by averaging spiking neuronal activity, individual spikes and changes in synaptic weights caused by coincident spiking are stochastic processes. Our results indicate how the stochasticity can be instrumental in optimization of visual performance.

Second is the fact that the capacity of individual neurons for estimating stimulus parameters is associated with *uncertainty of measurement* (Gabor, 1946, 1952; Cherry, 1978; Marcelja, 1980; Daugman, 1985; Resnikoff, 1989). In particular, receptive fields of different sizes are useful for measuring different aspects of stimulation (Gepshtein, Tyukin, & Kubovy, 2007). Small receptive fields are useful for localization of stimuli, i.e., for measuring stimulus location, whereas large receptive fields are useful for measuring stimulus frequency content. Thus, *the size of receptive field* should be an important parameter for optimizing system behavior.

We investigate consequences of stochastic fluctuations in receptive field size using numerical simulations and analysis. Numerically, we model plasticity of synaptic weights in generic neural circuits and find that the plasticity is accompanied by fluctuations of receptive field size and that the amplitude of fluctuations co-varies with receptive field size. Analytically, we use standard stochastic methods (Gardiner, 1996) to explore consequences of such fluctuations in neuronal populations.

We find that the fluctuations can steer receptive fields of multiple neurons toward a stable state that is remarkable in two respects. First, the distribution of receptive field sizes supports a distribution of spatiotemporal visual sensitivity that is strikingly similar to that observed in the human vision (Kelly, 1979), illustrated in Fig. 1. Second, the distribution of receptive field sizes in the population is consistent with prescriptions of a model of efficient allocation of receptive fields in the human visual system (Gepshtein et al., 2007), where errors of measurement are minimized across all receptive fields.

Local dynamics

Uncertainty of measurement

Uncertainty principle—The capacity of individual neurons for estimating stimulus location and frequency content is limited by a constraint known as the “uncertainty principle" (Gabor, 1946, 1952) or “uncertainty principle of measurement" (Resnikoff, 1989). According to this principle, the uncertainties associated with measuring the location and frequency content of the signal over some interval Δx (spatial or temporal) are not independent of one another:

$$U_x U_{\tilde{x}} \geq C, \quad (1)$$

where U_x is the uncertainty of measuring signal location within Δx, U_x is the uncertainty of measuring the variation of signal over Δx (which is the “frequency content" of the signal on Δx), and C is a positive constant. Equation 1 implies that, at the limit of measurement ($U_x U_{\tilde{x}} = C$), the two uncertainties trade off: decreasing one uncertainty can only be accomplished by increasing the other.

The uncertainty principle has proven to be most useful for understanding function of individual visual neurons in the primary visual cortex. The neurons were shown to implement an optimal tradeoff between the uncertainties associated with measurement of stimulus location and spatial frequency content (Marcelja, 1980; MacKay, 1981; Daugman, 1985; Glezer et al., 1986; A. J. Jones & Palmer, 1987).

Here we are concerned with consequences of the uncertainty principle for neuronal populations characterized by a broad range of spatial and temporal extents of receptive fields. Gepshtein et al. (2007) have recently undertaken an analysis of such a system. They considered an ideal case in which the neurons were allocated to stimuli such that the conditions of measurement with the same expected uncertainty would receive the same amount of neural resources. The analysis showed that a characteristic of performance expected in the ideal visual system had the same shape as a well-known characteristic of human contrast sensitivity: the *Kelly function* illustrated in Fig. 1. In particular, it was predicted that the position of the sensitivity function in the coordinates of Fig. 1 would depend on statistics of stimulus speed, but the shape of the function would be invariant under changes in stimulus statistics.

This view has been supported by a study of how motion adaptation changes contrast sensitivity across the entire domain of the Kelly function (Gepshtein, Lesmes, & Albright, 2013). The changes of contrast sensitivity formed a pattern similar to the pattern predicted for the ideal system. From this perspective, the sensitivity function and its adaptive changes result from an optimization process that mediates the efficient and flexible allocation of neurons, in accord with the expected uncertainty of measurement, and in face of the variable statistics of the environment.

Here we explore how this optimization can be implemented in visual systems. We address this question by, first, reviewing how the expected uncertainty of measurement varies in populations of neurons characterized by a wide range of spatial and temporal extents of their receptive fields.

Composite uncertainty of measurement—Consider a visual system in which the same neurons can be used for localizing stimuli and for measuring stimulus frequency content. As mentioned, at the limiting condition of measurement ($U_x U_x = C$), decreasing uncertainty about one aspect of measurement (say, location) is necessarily accompanied by increasing the other (frequency content). When written as a function of receptive field size, the joint uncertainty of measuring stimulus location and frequency content incorporates both tendencies, the increasing and the decreasing:

$$U_{j(X,\tilde{\mathrm{X}})} = \lambda_X X + \lambda_{\tilde{\mathrm{X}}} / X, \quad (2)$$

where λ_X and $\lambda_{\tilde{X}}$ are positive coefficients representing the relative importance of the two aspects of measurement and X is the size of the receptive field (spatial or temporal). This *uncertainty function* has a unique minimum, at which receptive fields are most suitable for concurrent measurement of stimulus location and frequency content (Gepshtein et al., 2007).

When measurements are performed in space and time, using receptive fields of spatial and temporal extent *S* and *T*, the joint uncertainties of separate spatial and temporal measurements are

$$U_{j(T,\tilde{\mathrm{T}})} = \lambda_T T + \lambda_{\tilde{\mathrm{T}}} / T, \; U_{j(S,\tilde{\mathrm{S}})} = \lambda_S S + \lambda_{\tilde{\mathrm{S}}} / S,$$

and the joint uncertainty of spatiotemporal measurements (which we call “composite uncertainty”) is

$$U_c = U_{j(T,\tilde{T})} + U_{j(S,\tilde{S})}. \quad (3)$$

The smaller the composite uncertainty of a receptive field, the more useful it is for jointly measuring location and frequency content of spatiotemporal stimuli. Receptive fields with equal uncertainty U_c are assumed to be equally useful for joint spatiotemporal measurements.

As mentioned, the expected utility of visual measurement could guide allocation of receptive fields of different spatial and temporal extents. Now we turn to the question of how this allocation can be implemented in terms of basic properties of neuronal circuits. We start by scrutinizing the mechanisms that control the size of receptive fields in neural circuits, with an eye for how the function of such circuits is constrained by Gabor’s uncertainty principle.

Basic sensory circuit

We model a simple neural circuit in which the output receptive field size is controlled by weighted inputs from several cells with different receptive field sizes. In this circuit we implement a basic mechanism of neural plasticity (Hebb, 1949; Bienenstock, Cooper, & Munro, 1982; Paulsen & Sejnowski, 2000; Bi & Poo, 2001). We find that this mechanism alone is capable of adaptively adjusting the size of receptive field according to the task at hand. This adaptive tuning of receptive fields is enabled by stochastic fluctuations of the receptive field size, while the fluctuations are themselves a byproduct of circuit plasticity. The resulting dynamics of receptive field size follows a simple principle in which receptive field variability is a function of receptive field size.

We start with a circuit of which the measured characteristic is a receptive field on a single dimension x (Fig. 2*A*), which can be space or time. We first study how the circuit can be used to estimate stimulus location on x. We then generalize to joint measurement of stimulus location *and* frequency content on x, after which we consider joint measurement of location and frequency content in two dimensions (space and time).

Fig. 2A is an illustration of an elementary circuit used in our simulations and analysis. “Readout" cell $\mathscr{R}$ could be activated by two “input" cells $\mathscr{I}_1$ and $\mathscr{I}_2$ with receptive fields of different sizes on x. Receptive field size was defined as the standard deviation of stimulus locations on x that evoked cell responses: S_1 and S_2 for cells $\mathscr{I}_1$ and $\mathscr{I}_2$. For simplicity, we first considered receptive fields that fully overlapped, but which were not generally concentric. The stimuli were dynamic textures with natural spatial and temporal amplitude spectra (as explained in Appendix A).

Input cells could each be excited by stimuli falling within their receptive fields:

$$y_i(x) = \exp\left(-0.5(x/S_i)^2\right). \quad (4)$$

where y_i was the response of i-th cell, encoding the distance of the stimulus from the center of receptive field. In simulations of idealized neurons, values of y_i directly represented the strength of cell responses, and in simulations of Poisson neurons, values of y_i represented the rate of Poisson random variables (Appendix A). The maximum value of y_i was the same for all input cells and it was independent of size S_i of cell receptive field. Activation of input cells could lead to activation of the readout cell, modulated by input-readout weights w_i:

$$y_r = \begin{cases} 1, & \sum_i w_i y_i \geq \Theta \\ 0, & \text{otherwise,} \end{cases} \quad (5)$$

where y_r is the response of the readout cell and Θ is *response threshold* of readout cell. In effect, the size of readout receptive field depended on sizes of input receptive fields (here S_1 and S_2), such that $S_1 \leq S_r \leq S_2$. (The size of the readout receptive field, S_r, was computed as explained in Appendix A, Equation 15.)

Response threshold Θ in Equation 5 depended on recent stimulation:

$$\Theta = \sum_{k=-K+1}^{0} \mathbf{y}_r^{(k)} / K, \quad (6)$$

where k is a serial index of stimuli with $k = 0$ indicating the most recent one. That is, threshold Θ is a running average of K most recent responses of the readout cell. (In the simulations for Fig. 3, K was set to 50.) This way we implemented “metaplasticity" (i.e., adaptive plasticity; Bienenstock et al., 1982; Abraham & Bear, 1996). Threshold Θ fluctuated around a constant value while stimulation was stationary (Fig. 3B), but Θ rapidly changed its value as stimulation changed, ensuring that several input cells (two input cells in Fig. 2) had to be activated together to evoke a readout response.

We studied how plasticity of input-readout connections affected the receptive field size of readout cell. In numerical simulations, we had the input-readout synaptic weights w_i depend on the relative timing of presynaptic and postsynaptic spiking activity (Hebb, 1949; Paulsen & Sejnowski, 2000; Bi & Poo, 2001). Weights increased when a spike of input cell coincided with (fell within a short interval of) a spike of readout cell:

$$\Delta w_i = \varepsilon c_i - \tau w_i, \quad (7)$$

where c_i was the *coincidence rate*: the fraction of input spikes that coincided with readout spikes (Equation 14) and ε was a positive constant. Weight increments were balanced by exponential decay of weights at a rate determined by constant $\tau > 0$ (Bienenstock et al., 1982).

Readout cells tended to co-fire more with input cells whose receptive fields were small rather than large. This is illustrated in Fig. 3. Panel A is a comprehensive map of coincidence rates: c_1 (for cells $\mathscr{I}_1$ and $\mathscr{R}$; left panel) and c_2 (for cells $\mathscr{I}_2$ and $\mathscr{R}$; right panel):

- Rate c_1 was high for all combinations of weights w_1 and w_2. This is because the receptive field of $\mathscr{I}_1$ was encompassed by the receptive field of $\mathscr{I}_2$, activation of $\mathscr{I}_1$ was always accompanied by activation of $\mathscr{I}_2$, and so the joint activation of $\mathscr{I}_1$ and $\mathscr{I}_2$ led to activation of $\mathscr{R}$. But activation of $\mathscr{I}_2$ alone was insufficient to activate $\mathscr{R}$, as is illustrated in the right panel of Fig. 3A.
- Rate c_2 was high only for some combinations of w_1 and w_2. Since coincidence c_1 was larger than coincidence c_2 for most combinations of weights, weight w_1 was incremented more often than weight w_2, making S_r on average more similar to S_1 than to S_2.

The ensuing receptive field dynamics was characterized by two prominent tendencies. First, readout receptive field size S_r fluctuated between the smallest and largest input receptive field sizes with a clear central tendency, S_r^*, which we called the *preferred size* of the readout receptive field, illustrated in Fig. 2*B–C*. Second, the amplitude of fluctuation of S_r

was a function of proximity of S_r to S_r^*: the closer to S_r^* the smaller the amplitude, as illustrated in Fig. 2*C*.

Steady-state behavior of this circuit was remarkably stable, summarized in the graph of input-readout weights w_1 and w_2 in Fig. 4. Having started with different distributions of the weights, represented by the grid of arrows in Fig. 4, we found that in the long run the weights converged to the same vicinity of the weight space, marked by the gray circular outline. At the steady-state, weight w_1 was larger than weight w_2, underlying the aforementioned results of $S_1 > S_2$.

Measurement of location—The above behavior of the elementary circuit can be thought of as a competition of input cells for control of the readout cell. We have observed above that the input cell with a smaller receptive field won the competition, and so the readout receptive field size tended to be small. This behavior is consistent with the aforementioned fact that small receptive fields are generally more suitable for measuring stimulus location than large receptive fields. We therefore consider the above circuit as an implementation of this tendency.

Measurement of frequency content—In contrast, large receptive fields are more suitable than small ones for measurement of stimulus frequency content. We next studied measurement of stimulus frequency content with the same circuit. We found that now the input cell with a larger input receptive field won the competition, and so the readout receptive field size tended to be large.

In the following paragraphs, we illustrate this by first considering measurement of frequency content alone, disregarding measurement of stimulus location, and then we turn to effects of jointly measuring stimulus location and frequency content (Fig. 4B).

The size of input receptive fields in frequency domain f_x is reciprocal to its size on x, which is why responses of input cells to stimulation in the frequency domain were defined as

$$z_i(f_x) = \exp\left(-0.5(fS_i)^2\right). \quad (8)$$

As in Equation 4, values of y_i either represented the strength of cell responses directly (in simulations of idealized neurons) or they represented the rate of Poisson random variables (in simulations of Poisson neurons) as detailed in Appendix A. Applying the same method of updating input-readout weights as above (Equation 7), we found that now readout receptive field size (S_r) tended toward the larger input receptive field size on x (S_2). That is, S_r tended toward the smaller input size on f_x, but because of the reciprocity of receptive field sizes on x and f_x, the tendency toward a smaller size on f_x was manifested as a tendency toward a larger size on x.

This behavior is summarized in Fig. 4B, in the graph of input-readout weights (pink outline and histogram). As before, steady-state behavior of the circuit was remarkably stable, but now weight w_1 was lower than weight w_2, underlying the aforementioned results of $S_1 < S_2$.

To sum up, when readout receptive fields measured either stimulus location alone or frequency content alone, their evolution led to opposing tendencies in receptive field size: for measurement of location they tended to become smaller and for measurement of frequency content they tended to become larger. In both cases, readout receptive field sizes fluctuated around their preferred values: the farther from the preferred value the larger the amplitude of fluctuation (Fig. 5).

Joint measurement of location and frequency content—Next we studied the behavior of the basic circuit of which the input cells were activated by stimuli that varied in two parameters: location x and frequency content f_x. Input cell response was defined as

$$yz_i(x, f_x) = y_i(x) z_i(f_x). \quad (9)$$

where $y_i(x)$ and $z_i(f_x)$ were as in Equations 4 and 8. Resulting preferred weights w_1 and w_2 are summarized in Fig. 4*B* and dynamic of receptive field size S_r is summarized in Fig. 5. The values of weights and receptive field sizes fell in between those observed when only stimulus location or only stimulus frequency content were taken into account.

Equation 9 is a general description of circuit behavior, of which the conditions captured by Equations 4 and 8 are special cases. Circuit dynamics for all the regimes of measurement considered above is summarized in Fig. 4*B* and Fig. 5. In Fig. 4*B* we plotted the convergence regions and histograms of weights obtained during numerical simulations of circuit dynamics. To summarize, preferred weights depended on the nature of events that activated input cells, and so did preferred readout sizes S_r (Equation 15) as shown in Fig. 5. Notably, we found that in every case readout receptive field size S_r fluctuated such that the amplitude of fluctuation varied as a function of S_r.

Circuit generalization

The uncertainty principle for receptive fields—Behavior of the neural circuit introduced in Fig. 2 can be summarized as follows.

- Input cells are vying for control of the readout cell, as they measure the location and frequency content of stimuli impinged on their overlapping receptive fields.
- The input cell with the smallest receptive field tends to win the competition when stimulus location is the only factor, because activation of such a cell is on average a more reliable indicator of stimulus location than activation of cells with larger receptive fields.
- Conversely, the input cell with the largest receptive field tends to win the competition when stimulus frequency content is the only factor.
- When these factors are combined, advantages and disadvantages of small and large receptive fields drive the readout receptive fields toward an intermediate size.

This behavior is expected in a system constrained by the uncertainty principle of measurement (Equation 1). Readout receptive fields in our simulations tended to be small or large when we considered, respectively, only the location or only the frequency content of the stimulus, and they tended to be of intermediate size when both stimulus location and frequency content were taken into account, as if the circuit was optimized according to the uncertainty principle.

Key features of circuit behavior observed in the elementary case of Fig. 2 held across a very broad range of circuit configurations. Circuit dynamics captured by Fig. 5 was found whenever multiple input cells with different receptive field sizes responded to the same stimuli (characterized by the same x and/or f), and whenever readout threshold was such that readout cell activity depended on multiple input cells, whether the input receptive fields overlapped fully or partially. The dynamics did not depend on the shapes of weighting functions for input receptive fields, on whether the input receptive fields were fixed or their sizes varied, or on whether spiking activity was noisy or not (as long as the noises on input cells were uncorrelated). The same dynamics was observed in circuits where input-readout weights decayed in the absence of spike coincidences (as described above) or the weights

were normalized, and also in circuits that consisted in many more cells than in Fig. 2, as we show next.

Measurement in space-time—Similar results held in circuits activated by more stimulus dimensions and using more input cells than in Fig. 4. For example, Fig. 6 summarizes the results of receptive field fluctuation in a circuit of which the input receptive fields overlap both in space and time, using 25 input cells (Appendix A). Here, not only the spatial and spatial-frequency aspects of stimuli were taken into account (as in the simulations represented in Figs. 4*B* and 5 in green), but also the temporal and temporal-frequency aspects. The coordinates in Fig. 6*A* represent the temporal (*T*) and spatial (*S*) extents of a receptive field. The two dotted grid lines intersect at the preferred readout receptive field size $\mathbf{X}_r^*=(T_r^*, S_r^*)$: a spatiotemporal generalization of the result indicated by the dashed lines in Fig. 5.

It is convenient to think of receptive field properties in terms of a balance of adaptive and conservative tendencies. The adaptive tendency is manifested by fluctuation of receptive fields, underlying flexible and efficient allocation of receptive fields, as we show below. Yet this flexibility must take place against a background of conservative processes; otherwise the visual system would be unprepared for sensing stimuli that are generally important but which are absent in the current stimulation. In the simulations for Fig. 6, the readout cell was set to preserve some of its properties. We implemented this by enhancing one of the input weights, which made the size of the readout receptive field tend toward a point in (*T*, *S*) marked by the white cross in Fig. 6: the original size (T_0, S_0) of the readout receptive field in all simulations for Fig. 6.

Independently of initial conditions, the simulations yielded a highly consistent result, summarized in Fig. 6*A*. The plot is a map of the probabilities of $\mathbf{X}_r$ in the course of one numerical simulation. Preferred size $\mathbf{X}_r^*$ is the point in (*T*, *S*) at which the probability has the highest value, marked by the intersection of white dotted lines. On multiple iterations, each starting at the initial condition marked by the white cross, the readout receptive field invariantly tended to the same preferred size $\mathbf{X}_r^*$. The same result was obtained when the initial conditions were selected for every iteration at random.

In the simulations for Fig. 6*A*, the distribution of stimuli was uniform. Next, we studied how biases in stimulation affect the preferred size of readout receptive field. The distribution of speeds in the natural stimulation is not uniform (e.g., Dong & Atick, 1995; Betsch, Einhäuser, Körding, & König, 2004). In the simulations for Fig. 6*B*– *D*, the prevalent speed of stimulation increased from low to high, indicated by the probability density function plotted at top right of each panel. The preferred receptive field size of the readout cell shifted towards the receptive field size of input cells tuned to speed similar to the prevalent speed. As the prevalent speed increased, the preferred size of the readout receptive field shifted further toward the prevalent speed. That is, in panel *B*, where the prevalent speed was low, the preferred readout size shifted toward the bottom right corner of the graph. And in panel *D*, where the prevalent speed was high, the preferred readout size shifted toward the top left corner.

Overall, behavior of the basic circuit can be summarized in terms of a tradeoff of stability and variability. On the one hand, readout receptive field tends toward a fixed size: preferred size $\mathbf{X}^*$ biased toward the more likely stimuli. On the other hand, the size of the readout receptive field fluctuates in a manner that can be characterized by a functional relation between the expected change of readout receptive field size (the “amplitude of fluctuation”) and the distance of current readout size from the preferred readout size $|\mathbf{X} - \mathbf{X}^*|$. We summarize this relationship as

$$E[\Delta \mathbf{X}] \sim f(\mathbf{X}), \quad (10)$$

where $E[\Delta \mathbf{X}]$ is the expected amplitude of fluctuation and $f(\mathbf{X})$ is a function with a single global minimum, as in Fig. 5.

Global dynamics

In the previous section, we associated the stimulus-dependent plasticity of neural circuits with random fluctuations and drifts of receptive field size. We found that the dynamics of receptive field size was described by a function motivated by Gabor's uncertainty principle. We have also found that the distribution of receptive field characteristics depended on the the statistics of stimulation.

Now we turn to a different level of modeling and consider neuronal plasticity in terms of ensemble dynamics. We will model an ensemble of neurons for which we examine steady-state distributions of receptive field characteristics. We will see that the allocation of receptive fields derived from the stochastic formulation is remarkably similar to the allocation found in biological vision and consistent with predictions of efficient allocation (Fig. 1).

Model of global dynamics

Amplitude of size fluctuation—Given the definition of measurement uncertainty that applies to the entire range of receptive field spatial and temporal extents (Equation 3), our model of receptive field size fluctuation must capture the association of measurement uncertainty and amplitude of fluctuation across an equally broad domain. The general form of this association is

$$E[\Delta \mathbf{X}] \sim \mathscr{F}[U_c(\mathbf{X})],$$

where U_c is the composite uncertainty (Equation 3) and $\mathscr{F}[\cdot]$ is an operator that establishes the correspondence between properties of uncertainty and properties of receptive field size fluctuations. We considered operator $\mathscr{F}$ generated by random walks of this form:

$$\Delta \mathbf{X} = \gamma U_c(\mathbf{X}) \mathbf{R}, \quad (11)$$

where $\mathbf{R}$ is a random process sampled from a bivariate normal distribution, and γ is a positive constant that represents the rate at which measurement uncertainty U_c affects the fluctuation. Below we show that on this formulation, fluctuation of readout receptive field size has the desired properties (Equation 13).

Random process $\mathbf{R}$ in Equation 11 can be thought of as a model of stochastic motion of point $\mathbf{X}_i = (T_i, S_i)$ on plane (T, S). Changes of $\mathbf{X}_i$ in regions of high uncertainty are on average larger than in regions of low uncertainty, having the effect that points $\mathbf{X}_i$ drift toward regions of low uncertainty, as illustrated in Figs. 7–8. In Appendix B we demonstrate that this behavior is predicted by a model in which fluctuation of receptive field size is formalized as a continuous-time stochastic process.

Biases of fluctuation—Measurement uncertainty is intrinsic to the visual system: it does not depend on stimulation. But outcomes of measurement also depend on properties of stimulation: an extrinsic factor. Under natural conditions, stimulus speeds are not distributed

evenly (e.g., Dong & Atick, 1995; Betsch et al., 2004) making neurons with certain speed preferences more useful in one environment than another.

As we saw in our analysis of the basic circuit, receptive field fluctuations are sensitive to biases in stimulation (Fig. 6). The shift of preferred size toward the prevalent speed (line $S = \nu_e T$ for prevalent speed ν_e) in the parameter space causes that the region of size fluctuation narrows in the direction orthogonal to this line. In other words, random process **R** in our definition of operator $\mathscr{F}$ is generally anisotropic: the "steps" of $\mathbf{X}_i$ in the different directions on the plane are not equally likely. The changes in spatial and temporal extents of receptive fields are correlated, so that "movements" of receptive fields in the space of parameters are constrained to specific trajectories. The trajectories are lines with slopes determined by cells' estimate of expected speed in the environment (see section *Organization of dynamics* below).

Constraints on dynamics

By the nature of input-readout connectivity, fluctuations of receptive fields are confined to some vicinity of the initial receptive field sizes:

$$\mathbf{X} \in \Omega_{\mathbf{X}_0}, \quad (12)$$

where $\Omega_{\mathbf{X}_0}$ is a connected and bounded region in $\mathbb{R}^2$, with reflecting boundary $\partial\Omega_{\mathbf{X}_0}$, and where $\mathbf{X}_0$ is the original size of the receptive field. The "reflecting" boundary means that, if **X** were to escape $\Omega_{\mathbf{X}_0}$, **X** was assigned a value inside the boundary as if **X** was reflected from $\partial\Omega_{\mathbf{X}_0}$ (Appendix B).

Joint effects of adaptive and conservative tendencies in allocation of receptive fields are illustrated in Fig. 7, for small regions in the receptive field parameter space (*T*, *S*). Panel *A* illustrates the effects of measurement uncertainty alone, and panel *B* illustrates how effects of measurement uncertainty are modulated by statistics of stimulation.

Range of fluctuation—In panel *A*, receptive fields are represented as points $\mathbf{X}_i = (T_i, S_i)$. The region circumscribed by the yellow boundary is the *range of fluctuation* (Equation 12). It represents the conservative tendency of receptive field size. All the receptive fields shown in this figure had the same initial parameter values and all underwent an equal number of stochastic changes. The final parameter values of receptive fields are marked by red points ("end points"). The evolution of three receptive fields are visualized as trajectories in the parameter space represented by series of connected black arrows. Arrow sizes illustrate the basic feature of this approach that the variability of receptive fields depends on their measurement uncertainty (Equation 11).

As mentioned in section Approach, receptive fields $\mathbf{X}_i$ tend to drift toward regions in the parameter space where measurement uncertainty is low (light regions in the background of Fig. 7*A*). This tendency is manifested by the high concentration of end points near the boundary of the range of fluctuations, toward the minimum of measurement uncertainty.

Local tendency—The distribution of end points is also plotted in Fig. 7*A*, as a normalized histogram (inset). The peak of distribution is the *local tendency* of this stochastic process within the range of fluctuations, determined by measurement uncertainty alone. (In Fig. 8*A* we depict such local tendencies for many locations in the parameter space.)

We validated the results of computational experiments in a steady-state analysis of receptive field fluctuations. The steady state is understood here as the time-invariant solution of a Fokker-Plank equation (Gardiner, 1996) with zero drift and diffusion coefficients that

depend on local measurement uncertainty $U(\mathbf{X})$. The results of our simulations are consistent with the analytic prediction: the asymptotic distribution of the probability density of receptive field parameters $\mathbf{X}$ is

$$p(\mathbf{X}) \sim 1/U(\mathbf{X})^2. \quad (13)$$

In other words, the stochastic process tends to distribute receptive fields according to their measurement uncertainty $U(\mathbf{X})$, such that the maximum of $p(\mathbf{X})$ occurs at the minimum of $U(\mathbf{X})$ (Appendix C).

Effects of stimulus speed—Besides the intrinsic factors, outcomes of receptive field fluctuations also depend on regularities of stimulation. Fig. 7*B–D* illustrates local tendencies of receptive field fluctuation under three different prevailing speeds of stimulation (increasing from left to right), in the same form as the inset of panel *A*. Evidently, local tendencies depend on the prevailing speed: the higher the prevailing speed the steeper the direction from the initial receptive field size to the mean end point of fluctuations. The local tendencies are depicted in the top panels of Fig. 7*B– D* by directed markers, each made of a filled circle at the initial parameters of receptive fields, from which a line is drawn to the mean end point of fluctuations.

Organization of dynamics

Fig. 8*A* is a summary of the local tendencies of receptive field fluctuation across the entire parameter space (*T, S*). Each local tendency is represented by a marker directed from initial parameters of receptive fields to the mean end points of their fluctuations, as explained in Fig. 7*B*. The markers form a global pattern with features as follows.

Pathlines—The local tendencies form a flow field that consists of distinct “streaks" which we call *pathlines*. In Fig. 8*A* we illustrate this notion by isolating a set of markers (highlighted in red). If not for the conservation of receptive field size (Equation 12), receptive field representations contained in the highlighted region would “travel" up and down along the pathlines.

The pathlines could be constructed by iteration, placing new initial parameters of receptive fields in the previous mean end points. The pathlines can also be derived analytically from Equations 11–12 as we show in Appendix C.

Optimal set—Fig. 8*A* illustrates how the local tendencies within pathlines switch directions in mid-path. All the switch points across the pathlines form a curve shown in the figure in gray and white. This curve is notable in two respects: (1) If not for the conservation of receptive field size (Equation 12), the receptive fields would all converge on the curve. We indicate this in Fig. 8*A* by the white segments of the curve, where receptive fields from the zones highlighted in red would converge. (2) The curve is also the optimal set of speed measurement (“optimal set") predicted by a theory of efficient resource allocation (Gepshtein et al., 2007) (Appendix C).

Fig. 8*B – C* illustrate the outcomes of receptive field size fluctuations using the density histograms introduced in Fig. 7. Fig. 8*B* is a histogram for receptive fields that belong to the pathlines shown in Fig. 8*A* in red. The histogram indicates that the receptive fields tend to concentrate near the optimal set of speed measurement (the gray curve).

Fig. 8*C* is a histogram for all the receptive fields. The distribution of receptive field density has a pattern similar to the one predicted by the theory of efficient resource allocation (Fig.

1*A*) and it corresponds to the pattern of motion sensitivity observed in human vision (Kelly, 1979).

Discussion

We used an idealized visual system to investigate how visual sensitivity is controlled in face of noisy neural mechanisms and variable stimulation. We implemented generic properties of neuronal plasticity and explored regularities of the ensuing local and global dynamics of neuronal receptive fields. We found that the noisy variation of receptive fields is in fact beneficial to system's performance. The stochastic changes of receptive fields and regularities of stimulation jointly steer neuronal ensembles toward an efficient distribution of receptive fields. This distribution is predicted by a theory of efficient allocation of receptive fields, and it is consistent with a well-known behavioral characteristic of spatiotemporal sensitivity in human vision (Fig. 1*A*).

Previous studies suggested that the observed distribution of visual sensitivity is a result of optimization of measurement by large neuronal ensembles (Watson, Barlow, & Robson, 1983; Gepshtein et al., 2007, 2013). Here we proposed a simple mechanism for how such optimization can be attained. Notably, the efficient allocation of receptive fields in multiple motion-sensitive cells emerges in a process that is purely local and unsupervised.

The optimization has a *local genesis* in that the fluctuation of receptive field properties in every cell is independent of fluctuations in other cells. The optimization is driven only by the local measurement uncertainty and by the individual stimulation of every cell.

The optimization is *unsupervised* in that it unfolds without having the statistics of stimulation explicitly represented in the system, and in that this process requires no agency or specialized system for coordinating the allocation of receptive fields. In other words, the efficient allocation is an outcome of neuronal self-organization. The stochastic behavior of multiple cells results in a "drift" of their receptive fields in the direction of low uncertainty of measurement, as if the system sought stimuli that could be measured reliably (*cf*. "infotaxis" in Vergassola et al., 2007 and minimization of free energy in Friston et al., 2009). Such behavior makes the system highly flexible and able to rapidly adapt to the changing environment, differently for different aspects of stimulation (*cf*. de Ruyter van Steveninck et al., 1994).

Stochastic methods have been successfully used in modeling dynamics of neural cells and cell populations (Harrison, David, & Friston, 2005; Knight, 2000; Ernst & Eurich, 2002; Dayan & Abbott, 2005). Such models addressed very fast processes: from activation of individual ion channels to generation of spikes and spike trains. These models helped understanding how elementary (microscopic) neural events add up to macroscopic phenomena (such as evoked response potentials; Harrison et al., 2005). Here we used stochastic methods to investigate neural events on a much slower temporal scale: variation of cell responses manifested in their receptive fields.

Theories of sensory optimization belong on a spectrum between stimulus-bound and system-bound extremes. On the stimulus end of this spectrum, the emphasis is on efficient representation of stimuli, such as in theories of efficient coding (where neuronal selectivity is conceived as the basis of efficient decomposition of stimuli, e.g., Barlow, 1961; Olshausen & Field, 1996; Bell & Sejnowski, 1997) and in theories of perceptual inference (where prior representation of stimulus parameters is key, e.g., Simoncelli & Olshausen, 2001; Geisler, 2008; Maloney & Zhang, 2010). On the system end, theories are primarily concerned with intrinsic properties of neural systems, such as dynamics of neuronal

populations (Sutton & Barto, 1981; Gong & van Leeuwen, 2009; Friston & Ao, 2011; van den Berg et al., 2012) and receptive fields (Tsodyks et al., 1997; Ozeki et al., 2009).

The present study has gravitated toward the system end of the spectrum since previous work showed that intrinsic constraints of sensory measurement are sufficient to explain the large-scale sensory characteristics in question (Gepshtein et al., 2007, 2013). Here we found, in addition, that the noise intrinsic to neural systems can be instrumental in sensory systems tuning themselves for changes in stimulation (*cf*. Rokni, Richardson, Bizzi, & Seung, 2007in motor systems). We propose that fluctuation of receptive field size is a means of *stochastic optimization* of neural function (*cf*. Spall, 2003; Ermentrout, Galan, & Urban, 2008; Faisal, Selen, & Wolpert, 2008; called “stochastic facilitation” in McDonnell & Ward, 2011).

As in some studies mentioned above (e.g., Knight, 2000), we considered a system of uncoupled elements. Even though the efficient allocation of receptive fields is possible without cell communication, efficiency of this system could be improved by having cells interact. On the one hand, receptive fields themselves result from computations both within individual neurons (Jia et al., 2010; Segev & London, 2002; London & Häusser, 2005) and within neural circuits (Bishop & Nasuto, 1999; Laughlin & Sejnowski, 2003). On the other hand, cell assemblies afford more precise and expeditious estimation of sensory uncertainties than individual cells (Johnson, 2004; Knill & Pouget, 2004).

Future work should investigate effects of cell coupling on self-organization and optimization of sensory systems, in particular the additional degrees of flexibility that cell communication is expected to provide. For example, having cells with similar tuning characteristics inhibit one another will help the system to “even out" the distribution of receptive fields, thus preventing drain of resources from some less common but useful stimuli. In contrast, having cells with different tuning characteristics excite one another will expedite convergence to system’s optimal state: a behavior known as “swarm optimization" (Kennedy & Eberhart, 1995; Pratt & Sumpter, 2006).

Acknowledgments

We thank K. J. Friston, J. Snider and S. Saveliev for helpful comments about an earlier version of this manuscript. This work was supported by the Kavli Foundation, the Swartz Foundation, NSF 1027259, NIH EY018613, ONR MURI N00014-10-1-0072, the Royal Society International Joint Research Grant JP080935, and an Odysseus grant from the Flemish Organization for Science FWO.

References

Abraham WC, Bear MF. Metaplasticity: the plasticity of synaptic plasticity. Trends in Neuroscience. 1996; 19:126–130.

Barlow, HB. Possible principles underlying the transformations of sensory messages. In: Rosenbluth, WA., editor. Sensory communication. Cambridge, MA, USA: MIT Press; 1961.

Barlow HB. Pattern recognition and the responses of sensory neurons. Annals of the New York Academy of Sciences. 1969; 156:872–881. [PubMed: 5258022]

Bell A, Sejnowski TJ. The ‘independent components’ of natural scenes are edge filters. Vision Research. 1997; 37:3327–3338. [PubMed: 9425547]

Betsch BY, Einhäuser W, Körding KP, König P. The world from a cat’s perspective – statistics of natural videos. Biological Cybernetics. 2004; 90(1):41–50. [PubMed: 14762723]

Bi G, Poo M. Synaptic modification by correlated activity: Hebb’s postulate revisited. Annual Review of Neuroscience. 2001; 24:139–166.

Bienenstock EL, Cooper LN, Munro PW. Theory for the development of neuron selectivity: orientation specificity and binocular interaction in visual cortex. Journal of Neuroscience. 1982; 2:32–48. [PubMed: 7054394]

Bishop JM, Nasuto SJ. Communicating neurons–an alternative connectionism. Proceedings of the weightless neural network workshop, york, uk. 1999

Cherry, C. On human communication: a review, a survey, and a criticism. Cambridge, Massachusetts: MIT Press; 1978.

Dan Y, Dong D, Reid RC. Efficient coding of natural scenes in the lateral geniculate nucleus: Experimental test of a computational theory. Journal of Neuroscience. 1996; 16:3351–3362. [PubMed: 8627371]

Daugman JG. Uncertainty relation for the resolution in space spatial frequency, and orientation optimized by two-dimensional visual cortex filters. Journal of the Optical Society of America A. 1985; 2(7):1160–1169.

Dayan, P.; Abbott, LF. Theoretical neuroscience: Computational and mathematical modeling of neural systems. 1st ed.. The MIT Press; 2005.

de Ruyter van Steveninck RR, Bialek W, Potters M, Carlson RH. Statistical adaptation and optimal estimation in movement computation by the blowfly visual system. Proceedings of IEEE Conference on Systems, Man, and Cybernetics. 1994; 1:302–307.

Dong D, Atick J. Statistics of natural time-varying images. Network: Computation in Neural Systems. 1995; 6:345–358.

Duff, GFD. Partial differential equations. University of Toronto Press; 1956.

Ermentrout GB, Galan RF, Urban NN. Reliability, synchrony and noise. Thrends in Neuroscience. 2008; 31:428–434.

Ernst, UA.; Eurich, CW. Cortical population dynamics and psychophysics. In: Arbib, MA., editor. The handbook of brain theory and neural networks. Second edition. The MIT Press; 2002. p. 294-300.

Faisal AA, Selen LPJ, Wolpert M. Noise in the nervous system. Nature Reviews Neuroscience. 2008; 9:292–303.

Friston KJ, Ao P. Free energy, value, and attractors. Computational and Mathematical Methods in Medicine. 2011:1–27.

Friston KJ, Daunizeau J, Kiebel SJ. Reinforcement learning or active inference? PLoS ONE. 2009; 4(7):e6421. [PubMed: 19641614]

Gabor D. Theory of communication. Part 1: The analysis of information. Electrical Engineers - Part III: Radio and Communication Engineering, Journal of the Institution of. 1946; 93(26):429–441.

Gabor D. Lectures on communication theory. Technical report. 1952; 238 (Fall Term, 1951.).

Gardiner, CW. Handbook of stochastic methods: For physics, chemistry and the natural sciences. 2nd ed.. Springer; 1996.

Geisler WS. Visual perception and the statistical properties of natural scenes. Annual Review of Psychology. 2008; 59(1):167–192.

Gepshtein S, Lesmes LA, Albright TD. Sensory adaptation as optimal resource allocation. Proceedings of the National Academy of Sciences, USA. 2013; 110(11):4368–4373.

Gepshtein S, Tyukin I, Kubovy M. The economics of motion perception and invariants of visual sensitivity. Journal of Vision. 2007; 7(8):1–18. [PubMed: 18217853]

Glezer VD, Gauzel'man VE, Iakovlev VV. Principle of uncertainty in vision. Neirofiziologiia = Neurophysiology. 1986; 18(3):307–312. (PMID: 3736708). [PubMed: 3736708]

Gong P, van Leeuwen C. Distributed dynamical computation in neural circuits with propagating coherent activity patterns. PLoS Computational Biology. 2009; 5(12):e1000611. [PubMed: 20019807]

Harrison LM, David O, Friston KJ. Stochastic models of neuronal dynamics. Philosophical Transactions of the Royal Society of London. Series B, Biological Sciences. 2005; 360(1457): 1075–1091. (PMID: 16087449).

Hebb, DO. The organization of behavior. New York: John Wiley; 1949.

Heess N, Bair W. Direction opponency, not quadrature, is key to the 1/4 cycle preference for apparent motion in the motion energy model. The Journal of Neuroscience. 2010; 30(34):11300–11304. [PubMed: 20739550]

Hietanen MA, Crowder NA, Price NSC, Ibbotson MR. Influence of adapting speed on speed and contrast coding in the primary visual cortex of the cat. The Journal of Physiology. 2007; 584(Pt 2): 451–462. (PMID: 17702823). [PubMed: 17702823]

Jia H, Rochefort NL, Chen X, Konnerth A. Dendritic organization of sensory input to cortical neurons in vivo. Nature. 2010; 464(7293):1307–1312. (PMID: 20428163). [PubMed: 20428163]

Johnson DH. Neural population structures and consequences for neural coding. Journal of Computational Neuroscience. 2004; 16(1):69–80. (PMID: 14707545). [PubMed: 14707545]

Jones AJ, Palmer L. An evaluation of the two-dimensional Gabor filter model of simple receptive fields in cat striate cortex. Journal of Neurophysiology. 1987; 58(6):1233–1258. [PubMed: 3437332]

Jones MC, Marron JS, Sheather SJ. A brief survey of bandwidth selection for density estimation. Journal of the American Statistical Association. 1996; 91(433):401–407.

Kelly DH. Spatial frequency selectivity in the retina. Vision Research. 1975; 15(6):665–672. (PMID: 1138482). [PubMed: 1138482]

Kelly DH. Motion and vision. II. stabilized spatiotemporal threshold surface. Journal of the Optical Society of America. 1979; 69(10):1340–1349. [PubMed: 521853]

Kennedy J, Eberhart R. Particle swarm optimization. Neural networks 1995 proceedings., IEEE international conference on. 1995; Vol. 4:1942–1948.

Knight BW. Dynamics of encoding in neuron populations: some general mathematical features. Neural Computation. 2000; 12(3):473–518. (PMID: 10769319). [PubMed: 10769319]

Knill DC, Pouget A. The bayesian brain: the role of uncertainty in neural coding and computation. Trends in Neurosciences. 2004; 27(12):712–719. [PubMed: 15541511]

Krekelberg B, van Wezel RJA, Albright TD. Adaptation in macaque MT reduces perceived speed and improves speed discrimination. J Neurophysiol. 2006; 95(1):255–270. [PubMed: 16192331]

Laughlin SB, Sejnowski TJ. Communication in neuronal networks. Science. 2003; 301(5641):1870–1874. [PubMed: 14512617]

London M, Häusser M. Dendritic computation. Annual Review of Neuroscience. 2005; 28:503–532. (PMID: 16033324).

MacKay DM. Strife over visual cortical function. Nature. 1981; 289:117–118. [PubMed: 7453815]

Maloney LT, Zhang H. Decision-theoretic models of visual perception and action. Vision Research. 2010; 50(23):2362–2374. [PubMed: 20932856]

Marcelja S. Mathematical description of the response by simple cortical cells. Journal of the Optical Society of America. 1980; 70:1297–1300. [PubMed: 7463179]

McDonnell MD, Ward LM. The benefits of noise in neural systems: bridging theory and experiment. Nature Reviews Neuroscience. 2011; (7):415–426.

Moran J, Desimone R. Selective attention gates visual processing in the extrastriate cortex. Science. 1985; 229(4715):782–784. (PMID: 4023713). [PubMed: 4023713]

Nakayama K. Biological image motion processing: a review. Vision Research. 1985; 25(5):625–660. [PubMed: 3895725]

Nakayama K, Silverman GH. Detection and discrimination of sinusoidal grating displacements. Journal of the Optical Society of America. A, Optics and Image Science. 1985; 2(2):267–274.

Olshausen BA, Field DJ. Emergence of simple-cell receptive field properties by learning a sparse code for natural images. Nature. 1996; 381:607–609. [PubMed: 8637596]

Ozeki H, Finn IM, Schaffer ES, Miller KD, Ferster D. Inhibitory stabilization of the cortical network underlies visual surround suppression. Neuron. 2009; 62(4):578–592. [PubMed: 19477158]

Paulsen O, Sejnowski TJ. Natural patterns of activity and long-term synaptic plasticity. Current Opinion in Neurobiology. 2000; 10(2):172–180. [PubMed: 10753798]

Petrovski, IG. Ordinary differential equations. Prentice-Hall: 1966.

Pratt SC, Sumpter DJT. A tunable algorithm for collective decision-making. Proceedings of the National Academy of Sciences of the United States of America. 2006; 103(43):15906–15910. [PubMed: 17038502]

Resnikoff, HL. The illusion of reality. New York, NY, USA: Springer-Verlag New York, Inc; 1989.

Rodman HR, Albright TD. Coding of visual stimulus velocity in area MT of the macaque. Vision Research. 1987; 27(12):2035–2048. [PubMed: 3447355]

Rokni U, Richardson AG, Bizzi E, Seung H. Motor learning with unstable neural representations. Neuron. 2007; 54:653–666. [PubMed: 17521576]

Segev, I.; London, M. Dendritic processing. In: Arbib, MA., editor. The handbook of brain theory and neural networks. Second edition. The MIT Press; 2002. p. 324-332.

Seung H. Learning in spiking neural networks by reinforcement of stochastic synaptic transmission. Neuron. 2003; 40(6):1063–1073. [PubMed: 14687542]

Simoncelli EP, Olshausen B. Natural image statistics and neural representation. Annual Review of Neuroscience. 2001; 24:1193–1216.

Spall, JC. Introduction to stochastic search and optimization. New York, NY, USA: John Wiley & Sons, Inc; 2003.

Sutton RS, Barto AG. Toward a modern theory of adaptive networks: Expectation and prediction. Psychological Review. 1981; 88(2):135–170. [PubMed: 7291377]

Tsodyks MV, Skaggs WE, Sejnowski TJ, McNaughton BL. Paradoxical effects of external modulation of inhibitory interneurons. Journal of Neuroscience. 1997; 17:4382–4388. [PubMed: 9151754]

van den Berg D, Gong P, Breakspear M, van Leeuwen C. Fragmentation: loss of global coherence or breakdown of modularity in functional brain architecture? Frontiers in Systems Neuroscience. 2012; 6(20)

Vergassola M, Villermaux E, Shraiman BI. 'Infotaxis' as a strategy for searching without gradients. Nature. 2007; 445(7126):406–409. [PubMed: 17251974]

Vislay-Meltzer RL, Kampff AR, Engert F. Spatiotemporal specificity of neuronal activity directs the modification of receptive fields in the developing retinotectal system. Neuron. 2006; 50(1):101–114. (PMID: 16600859). [PubMed: 16600859]

Watson AB. Optimal displacement in apparent motion and quadrature models of motion sensing. Vision Research. 1990; 30(9):1389–1393. [PubMed: 2219754]

Watson AB, Ahumada AJ. Model of human visual-motion sensing. Journal of the Optical Society of America. A, Optics and Image Science. 1985; 2(2):322–341. (PMID: 3973764).

Watson AB, Barlow HB, Robson JG. What does the eye see best? Nature. 1983; 302:419–422. [PubMed: 6835375]

Womelsdorf T, Anton-Erxleben K, Treue S. Receptive field shift and shrinkage in macaque middle temporal area through attentional gain modulation. Journal of Neuroscience. 2008; 28(36):8934–8944. [PubMed: 18768687]

Appendix A

Details of numerical simulations

Stimuli

Unless stated otherwise, we used natural stimuli. The spatial and temporal amplitude spectra of natural stimuli followed a power law (function $1/f$) (Dong & Atick, 1995; Dan, Dong, & Reid, 1996). Stimuli were obtained using two methods: by extracting a single row of pixels from a movie of a natural scene or by generating a random stimulus for which the spectral amplitudes followed function $1/f$ and phases were drawn from a uniform distribution on interval $[0, 2\pi)$. Stimuli from both sources were then preprocessed. At low frequencies, stimulus spectra were flattened, simulating the output of retina and LGN (Barlow, 1969; Dan et al., 1996). Locations x and frequencies f of the stimuli that triggered input-cell responses (Equations 4 and 8) were determined by computing local maxima in the outputs of the convolution of stimuli with receptive field functions on x and f. Locations and frequencies obtained this way had near uniform distributions. To accelerate large-scale simulations, stimulus parameters (x, f) were drawn from uniform distribution on intervals that fully covered the largest receptive field of the input layer.

Stimulus speed was defined as ratio $\nu = f_t/f_s$ (Kelly, 1979). (Sets of pairs of f_t and f_s that correspond to the same ratio ν form constant-speed lines, as explained in Fig. 1*A*.) To derive amplitude spectra across speeds we integrated spatiotemporal spectra of the stimulus along the constant-speed lines. The distribution of amplitudes followed the $1/f$ function. Assuming the whitening of low frequencies (as in the domains of space and time), we obtained a uniform distribution of speeds.

Simulations of idealized neurons

Measurement in one dimension—The results summarized in Figs. 2–5 were obtained using a basic neural circuit that consisted of two input cells and one readout cell. Input receptive field sizes were $S_i \in \{1.0, 2.0\}$. On every iteration, random stimuli $\chi = (x, f)$, each characterized by location x and frequency content f, were sampled from a uniform distribution. Every time, we computed 10 cell responses yz_i (Equation 9) while the input-readout weights were kept constant. The readout cell generated a spike when the weighted sum of its inputs $\mathbf{y}_r = \sum_i w_i \mathbf{yz}_i$ exceeded threshold Θ. Threshold Θ was equal to the expected value of the weighted sum of input responses $\mathbf{y}_r$ during $K = 10$ most recent stimulations (Equation 6).

Weight w_i of i-th neuron was incremented by $\Delta w_i = \varepsilon c_i$, where $\varepsilon = 0.1$ and where

$$c_i = \frac{\sum_k \mathbf{yz}_i^{(k)} \mathbf{y}_r^{(k)}}{\sum_k \mathbf{yz}_i^{(k)}} \quad (14)$$

was the *coincidence rate* expressed as average of readout spikes (out of $K = 10$ most recent spikes) weighted by coincident responses of i-th input cell. The weight decayed with rate $\tau = 0.2$.

Effective sizes of readout receptive field

$$S_r = \frac{\sum_i w_i S_i}{\sum_i w_i} \quad (15)$$

were collected from $N_e = 20,000$ iterations in total. The normalized histogram of readout receptive field sizes is plotted in Fig. 4*B*. Values S_r were divided to $N_B = 31$ bins of equal size on range $[S_r^* - 0.05, S_r^* + 0.05]$. Changes of readout size $\Delta S_r = |S_r(j+1) - S_r(j)|$ were recorded separately for each bin. The average (expected) value of changes of receptive field size is plotted in Fig. 2*B*, only for bins that contained more than 0.5% of entries in the most populous bin.

Spatiotemporal measurement—The results of simulations described in this section are in Fig. 6. The same mechanisms of plasticity as for stimulus measurement in space were applied in Fig. 4 was applied in a circuit of 25 input cells and one readout cell, all having nested spatiotemporal receptive fields. Sizes of input receptive fields were sampled from a grid formed by five speeds $\nu \in \{1/4, 1/2, 1, 2, 4\}$ and five temporal sizes $T \in \{1/4, \sqrt{1/2}, 1/2, \sqrt{2}, 1\}$. Input-readout weights w_i were initialized such that original receptive field size was $\mathbf{X}_0 = (0.5, 0.5)$. Over the course of $N_e = 20,000$ epochs of simulation, stimuli were presented to input receptive fields (100 independently generated random stimuli $\chi = (x, f_x, t, f_t)$ per epoch), and weights w_i were updated according to Equation 7. Coincidence rate c_i was estimated over 100 stimulus presentations as in Equation 14.

Stimulus bias in the basic circuit—Stable-state input-readout weights depend on stimulus statistics. In Fig. 9 we illustrate this by plotting distributions of input-readout weights for different distributions of stimulus speeds. For this illustration, we considered input cells tuned to speed, with weighting functions

$$\omega_i(\nu_j)=\exp\left[-\frac{(\nu_j-\nu_i)^2}{2\nu_e^2}\right],$$

where ω_i is the tuning function of *i*-th input cell, ν_i is the tuning speed (i.e., the speed at which the tuning function has the highest value), and ν_j is a sample of stimulus speed. In contrast to the input-cell response function used previously (Equation 9), here the input response function was

$$yz_i(x,f_x)=\beta y_i(x)z_i(f_x)+(1-\beta)\omega_i(\nu_j), \quad (16)$$

where β is a constant ($0 \le \beta \le 1$) that determined the strength of speed tuning.

In Fig. 9, spiking activity of three input cells with sizes $S_i \in \{0.5, 1.0, 2.0\}$ encoded the distance of stimulus speed from the tuning speed of the cell ($\beta = 0.75$, Equation 16). Stimulus speed was sampled from three different distributions of stimulus speed shown on the bottom of Fig. 9 (green curves). The magnitudes of input-readout weights averaged over 5, 000 iterations in each of the three regimes of stimulation are plotted on top of Fig. 9.

Stimulus bias in the generalized circuit—In simulation of ensemble the effect of speed prevalence on circuit plasticity was implemented by introducing biases of weights w_i

- Conservatism of the *size* of receptive fields was implemented by giving advantage to the original input-readout weights at which readout receptive field size was $\mathbf{X}_0 = (T_0, S_0) = (0.5, 0.5)$:

$$\Delta w_i=\alpha_c w_i\exp\left[-\frac{(T_i-T_0)^2}{2T_0^2}-\frac{(S_i-S_0)^2}{2S_0^2}\right], \quad (17)$$

- Conservatism of the *speed preference* was implemented by giving advantage to those parameters of receptive fields at which spatiotemporal size ratio $\nu_i = S_i/T_i$ was similar to the prevalent (mean) speed of stimulation ν_e:

$$\Delta w_i=\alpha_\nu w_i\exp\left[-\frac{(\nu_i-\nu_e)^2}{2\nu_e^2}\right], \quad (18)$$

Constants (α_c, α_ν) are non-negative constants that control the degree of weight modulation. Their values for computation of conservative tendencies in the two cases were (0.05, 0) for panel *A*, and (0.05, 0.1) for panels *B* – *D*.

Simulations of Poisson neurons

Responses of input cells were modeled as homogeneous Poisson processes. Fig. 10 is an example of spike sequence from one such simulation. The normalized mean firing rate of an input cell was:

$$r_i = \exp\left(-0.5(x/S_i)^2\right),$$

where x is the distance of the stimulus from the center of the receptive field. For a cell with maximum firing rate $r_{\max}$, the normalized firing rate is $r_i = r_i^*/r_{\max}$, where r_i^* is the absolute firing rate, and the probability that n spikes occurred within interval Δt is governed by a Poisson distribution (Equation 1.29 in Dayan & Abbott, 2005). Coincidence rate c_i was computed using Equation 14 for binary input cell responses $yz_i \in \{0, 1\}$ and $K = 40$ (which includes the entire range of Fig. 10). Here the coincidence rate expresses the fraction of i-th input-cell spikes that coincided with readout spikes.

In the simulation for Fig. 10, input-readout weights were fixed at $w_1 = 0.3$ and $w_2 = 0.7$ (for the input cells with sizes $S_1 < S_2$) and readout threshold was $\Theta = 1.1 \times \max\{w_i\}$, ensuring that activation of one input cell was unlikely to trigger a readout spike in this illustration. This illustration makes it clear that readout spikes were triggered in two cases: when both input cells fired and when the input cell with the larger weight (here $w_2 = 0.7$) fired because of a slow decay of activity following a previous excitation.

Coincidence rate c_i is low for input cells that fire when other input cells do not. Low c_i is likely when a stimulus falls on the part of input receptive field that does not overlap with receptive fields of other input cells. The probability of such “isolated" spikes is high in circuits with large variability of input receptive field sizes, where small receptive fields overlap with only small parts of larger receptive fields. As a result, there is a monotonic relationship between receptive field size and input-readout weight: the smaller the input receptive field the larger its weight, supporting the notion that the circuit behaves as if it minimizes the uncertainty of measurement of location.

Size fluctuation

Fig. 7*A* is an illustration of the update rule of Equation 11. The contour plot in the background represents some uncertainty function of the form of Equation 3. Initial parameters of 1, 000 receptive fields were set to $\mathbf{X} = (0, 0)$. $\mathbf{R}$ was sampled from an isotropic normal distribution $\mathcal{N}(0, \mathbf{I})$, where $\mathbf{I}$ is an identity matrix.

Fig. 7*B–D* illustrate the conservation of tuning to speed. Receptive field fluctuations were confined to elliptic regions (Equation 25), the major axes of which were aligned with the locally estimated speeds ($\nu_i \in \{0.1, 1.0, 10.0\}$, respectively in panels *B, C* and *D*). The elliptic regions were centered at $\mathbf{X}_0 = (0, 0)$ and were defined as

$$\Omega_{\mathbf{X}_0} = \{\mathbf{X} \in \mathbb{R}^2 | \mathbf{X}^T A(\bar{\nu}_i)\mathbf{X} \leq 1\}, \quad (19)$$

where $A(\cdot)$ is an operator that controls the regions’ shapes and orientations (Appendix B). On this definition, domains $\Omega_{\mathbf{X}_0}$ change their orientations in response to changes in statistics of stimulation.

Pathlines

The pathlines in Fig. 8 have a simple analytic form derived in Appendix C (section *Derivation of pathlines*). For example, if $\bar{\nu}_i(\mathbf{X})$ is the expected speed of stimulation, ν_e, then the pathline through $\mathbf{X}_0 = (T_0, S_0)$ is

$$S=\nu_e T+C_0,$$

for $C_0 = S_0 - \nu_e T_0$ (Equation 31). The red curve in Fig. 8*B* represents such a pathline for one instance of $\mathbf{X}_0$.

Kelly function

Simulated Kelly function

Measurement uncertainty was as in Equation 3, with $\lambda_{i\in\{X,\tilde{T},\tilde{X},T\}} = \{0.012, 0.0013, 1.3234, 0.3\}$. Initial locations $\mathbf{X}_0$ were randomized to cover the parameter space uniformly. Receptive fields were first distributed across speeds according to probability distribution $p(\chi) \sim 1/U(\chi_i)$ where $\chi_\mathbf{i}$ are locations of minimal measurement uncertainty on cell pathlines. Expected speed $\nu_i(\mathbf{X}) = 0.353$ (Equation 24) was the same for all receptive fields, thus implementing the extreme case of all the cells having very large receptive fields, i.e., integrating speed on the entire open interval $\nu\in (0, \infty)$. Fluctuations of receptive field parameters T and S were according to Equation 11 with $\gamma = 0.1$ and $R_k \sim \mathcal{N}(0, 1)$. Fluctuations were constrained to bands in the parameter space described in section *Stochastic optimization of receptive field size* (Fig. 7), within boundaries centered on initial locations $\mathbf{X}_0$ such that $\|\mathbf{X} - \mathbf{X}_0\|^2 \leq 0.5\mathbf{X}_0$.

Because of the initial randomization of cell locations, some cells could not reach optimal locations by fluctuations alone: their fluctuation boundaries $\Omega_{\mathbf{X}_0}$ (Equation 12) did not contain minima of the uncertainty function. Such cells could still reach optimal locations, since $\mathbf{X}_0$ of all cells could change, although on a slow scale. Location $\mathbf{X}_0$ were updated to an estimate of local tendency within the previous fluctuation boundary after each N iterations (here $N = 50$). (The local tendencies were computed as in Fig. 7, except the steps of $\mathbf{X}$ were normalized by the amplitude of uncertainty change within $\Omega_{\mathbf{X}_0}$. The normalization insured that estimates of local tendency were comparable after equal numbers of iterations at different locations in the parameter space.) Only in the receptive fields removed from the minimum of uncertainty, the resulting changes of $\mathbf{X}_0$ were significant because there the differences between $\mathbf{X}_0$ and local tendencies were large. The imprecision (uncertainty) in estimation of local tendencies prevented the cells from lingering at the optimal locations, which is why the cells did not all converge at the minima of uncertainty. Changes of $\Omega_{\mathbf{X}_0}$ reached stable states after several thousands of iterations, whereas local tendencies (within $\Omega_{\mathbf{X}_0}$) reached stable states after tens of iterations.

Human Kelly function (Fig. 1A)

The contour plot of the human spatiotemporal sensitivity function (Fig. 1*A* and Equation 8 in Kelly, 1979) is rendered using a color map normalized by maximal sensitivity. The function was derived in the frequency domain (Kelly, 1979), here transformed to space-time using the fact that motion detectors are tuned to quarter-cycle displacement of moving stimuli (Nakayama, 1985; Gepshtein et al., 2007; Nakayama & Silverman, 1985; Watson, 1990; Heess & Bair, 2010). *Panel* B: The plot of sensitivity obtained by simulations described in section *Emergent contrast sensitivity characteristic* (Fig. 1B above.

Computations of density and sensitivity

Receptive field density was evaluated by linear superposition of two-dimensional Gaussian functions

$$e^{-\frac{1}{2}\left(\frac{T-T_i}{kT_i}\right)^2-\frac{1}{2}\left(\frac{S-S_i}{kS_i}\right)^2},$$

where (T_i, S_i) are receptive field parameters. The linear bandwidth parameter $k = 0.2$ was selected to obtain a smooth unimodal distribution of density (M. C. Jones, Marron, & Sheather, 1996).

The sensitivity was calculated by linear superposition of individual cell sensitivities (Kelly, 1979, 1975). The tuning of individual cells to spatial and temporal frequencies was assumed to have profile

$$\left(\frac{e}{f_0}\right)^2 f^2 e^{-2\left|\frac{f}{f_0}\right|},$$

where f_0 is the tuning frequency (Kelly, 1975). The sensitivity function was computed in the frequency domain and transformed to space-time as in Fig. 1.

Appendix B

Receptive field dynamics

We model systems of motion-sensitive neurons with receptive fields characterized by two parameters: spatial extent S and temporal extent T. We view these parameters as random processes that depend on the uncertainty of measurement by receptive fields:

$$\Delta\mathbf{X}=\gamma U(\mathbf{X})\mathbf{R}, \quad (20)$$

where

- $\Delta\mathbf{X} = (\Delta T, \Delta S)$ is a change of parameters $\mathbf{X} = (T, S)$,
- $U(\mathbf{X})$ is uncertainty of measurement,
- $\mathbf{R}$ is sampled from a bivariate normal random process, $\mathcal{N}0, 1)$,
- γ is a positive constant that represents the rate with which measurement uncertainty U affects parameter fluctuations.

In the following we derive an analytical prediction of the stable state of the described system.

Fluctuations in one dimension

For didactic reasons, we first consider fluctuations on one dimension, $X \in \mathbb{R}$. We rewrite Equation 20 as

$$X_{k+1}=X_k+\gamma U(X_k)R_k, \quad (21)$$

where R_k is a random process with zero mean. Receptive field size X is constrained to some range $\Omega_{X_0} : [x_{\min}\ x_{\max}]$, where $x_{\min}$ and $x_{\max}$ are reflecting boundaries (Gardiner, 1996). For sufficiently small γ, the fluctuations are approximated by a continuous-time stochastic model:

$$dX=U(X)dW,$$

where dW is an increment of a Wiener process $W(t)$ (Gardiner, 1996). By this process, X gets distributed according to the probability density function $p(X, t)$, a solution of this Fokker-Plank equation:

$$\frac{\partial p}{\partial t}=\frac{1}{2}\frac{\partial^2}{\partial X^2}U^2(X)p(X,t),$$

subject to boundary conditions. The stationary solution of this equation is

$$p_s(X)=\lim_{t\to\infty}p(X,t)=\frac{C}{U^2(X)}, \quad (22)$$

where C is such that

$$\int_{x_{\min}}^{x_{\max}}p_s(X)dX=1 \quad (23)$$

(Gardiner, 1996, p. 124). The maximum of this solution is obtained at the same X as the minimum of $U(X)$.

Fluctuations in two dimensions

Let receptive field parameters T and S vary according to Equation 20. Let the random process be constrained to regions $\Omega_{\mathbf{X}_0}$ in receptive field parameter space (T, S) (Equation 12), and let these regions have elliptical shapes whose centers are $\mathbf{X}_0$ and whose main diagonals are aligned with the locally expected speed of stimulation (Equation 24):

$$\bar{\nu}(\mathbf{X})=\frac{\int_0^\infty\omega(\nu,\mathbf{X})p(\nu)\nu d\nu}{\int_0^\infty\omega(\nu,\mathbf{X})p(\nu)d\nu}. \quad (24)$$

Speed $\bar{\nu}(\mathbf{X})$ represents an estimate of the expected stimulus speed. Sensor speed preference, $\omega(\nu, \mathbf{X})$, is biased by probability $p(\nu)$. The elliptic regions are then defined as:

$$\begin{aligned}\Omega_{\mathbf{X}_0}&=\{\mathbf{X}\in\mathbb{R}^2|(\mathbf{X}-\mathbf{X}_0)^T A(\mathbf{X}-\mathbf{X}_0)\le 1\},\\ A&=M\begin{pmatrix}1/a^2 & 0\\ 0 & 1/b^2\end{pmatrix}M^{-1},\\ M&=\begin{pmatrix}\cos(\theta) & -\sin(\theta)\\ \sin(\theta) & \cos(\theta)\end{pmatrix},\theta=\tan^{-1}(\bar{\nu}(\mathbf{X})),\end{aligned} \quad (25)$$

where a, b, $a^2 > b^2$ are the parameters of size and eccentricity of $\Omega_{\mathbf{X}_0}$. (On this definition, domains $\Omega_{\mathbf{X}_0}$ change their orientations as the stimulation changes.)

For small γ and $\mathbf{X} = [X_1, X_2]$, the random process is approximated by a continuous-time stochastic model:

$$dX_1=U(\mathbf{X})dW_1\ dX_2=U(\mathbf{X})dW_2,$$

where dW_1 and dW_2 are increments of Wiener processes $W_1(t)$ and $W_2(t)$. Now the Fokker-Plank equation is

$$\frac{\partial p}{\partial t}=\frac{1}{2}\left(\frac{\partial^2}{\partial X_1^2}+\frac{\partial^2}{\partial X_2^2}\right)U^2(\mathbf{X})p(\mathbf{X},t).$$

The stationary solution of this equation with reflecting boundary is unique. It is:

$$p_s(\mathbf{X})=\frac{C}{U^2(\mathbf{X})}, \quad (26)$$

where C is such that

$$\int_{\Omega_{\mathbf{X}_0}}\frac{C}{U^2(\mathbf{X})}d\mathbf{X}=1.$$

To see that, substitute $U(\mathbf{X})p_s(\mathbf{X})$ by $z(\mathbf{X})$. Function $z(\mathbf{X})$ must satisfy

$$\left(\frac{\partial^2}{\partial X_1^2}+\frac{\partial^2}{\partial X_2^2}\right)z(\mathbf{X})=0,\ \frac{\partial z}{\partial X_1}n_1(\mathbf{X})+\frac{\partial z}{\partial X_2}n_2(\mathbf{X})=0,$$

where vector $[n_1(\mathbf{X}), n_2(\mathbf{X})]$ is normal to the fluctuation boundary $\partial\Omega_{\mathbf{X}_0}$. The second equation just above is a consequence of the reflecting boundary condition (Gardiner, 1996, p. 146, section). From the Ostrogradsky-Gauss theorem it follows that the only general solution of the latter equations is $z(\mathbf{X}) = C$ (e.g., p. 99, *b–c* in Duff, 1956), where C is a constant uniquely determined by Equation 26.[1]

[1]Suppose that b is a differentiable function in $\mathbb{R}^2$, n is a unit normal to boundary $\partial\Omega$ of Ω and

$$\nabla\cdot b=\frac{\partial}{\partial X_1}b(X_1,X_2)+\frac{\partial}{\partial X_2}b(X_1,X_2).$$

According to the Ostrogradsky-Gauss theorem, the following identity must hold:

$$\int_\Omega \nabla\cdot b d\Omega=\int_\Omega \mathrm{div}(b)d\Omega=\int_{\partial\Omega} b\cdot n d\partial\Omega. \quad (27)$$

Let z and ν be any two functions each differentiable at least twice, and let $\Delta=\frac{\partial^2}{\partial X_1^2}+\frac{\partial^2}{\partial X_2^2}$. Then

$$\nu\Delta z+\nabla z\cdot\nabla\nu=\nabla\cdot(\nu\nabla z). \quad (28)$$

From Equations 28 and 27 it follows that

$$\int_{\Omega} \nu[\Delta z] d\Omega + \underbrace{\int_{\Omega} \nabla \nu \cdot \nabla z d\Omega}_{E(z,\nu)} = \int_{\Omega} \nabla \cdot (\nu \nabla z) d\partial\Omega = \int_{\partial\Omega} \nu \nabla z \cdot n d\partial\Omega.$$

Taking into account the reflecting boundary condition, $\nabla z \cdot n = 0$, and noticing that if z is a stationary solution then $\Delta z = 0$, we conclude that

$$E(z, z) = \int_{\Omega} \|\nabla z\|^2 d\Omega = 0.$$

Thus, given that function z is differentiable at least twice and that domain Ω is bounded, we conclude that $\nabla z = 0$ in Ω. Hence z must be a constant.

Boundary conditions

We derived the steady states of the stochastic processes by assuming a reflecting boundary condition. For consistency, we made the same assumption in the simulations of receptive field fluctuation. The “reflective boundary" implements a conservative trend of receptive field fluctuation. When a stochastic update brought receptive field parameters outside of the boundary: $\mathbf{X}_2 = \mathbf{X}_1 + \Delta\mathbf{X}$, where $\mathbf{X}_2 \notin \Omega_{\mathbf{X}_0}$, new parameters $\tilde{\mathbf{X}_2}$ were computed, as if the trajectory of receptive field change was reflected from the boundary Ω_{X_0} at point $\mathbf{X}_+$. This point was the intersection of line $\mathbf{X}_1\mathbf{X}_2$ and the boundary, such that

$$\tilde{\mathbf{X}}_2 = \mathbf{X}_2 - 2\mathbf{n}((\mathbf{X}_2 - \mathbf{X}_+) \cdot \mathbf{n}) \quad (29)$$

where $\mathbf{n}$ is the normal to the boundary at $\mathbf{X}_+$.

The choice of reflective boundary allowed us to simplify the analysis (Appendix C). Discrepancies between predictions of the analysis and results of simulations were most pronounced where the probability of “overstepping" the boundary was significant, i.e., at high fluctuation rates γ (Equation 20). For small γ, the effects of boundary condition on steady-state distribution of receptive field parameters was negligible.

The effect of fluctuation rate γ on convergence of receptive field parameters is illustrated in Fig. 11, in one dimension. The analytic prediction of steady state and results of computational experiments are shown for a system with a simplified uncertainty function, $U(X) = X^2 + 0.1$, using the update rule of Equation 21. The prediction is represented by the red line, computed as in Equation 22. (Here, the condition of Equation 23 is satisfied for $C \approx 8$.) Results of computational experiments are represented by the black curves, for four values of γ, having all the cells initialized to the same $X(t = 0) = 0.0$ in every case. Results of experiments agree with the analytic prediction when γ is small.

Appendix C

Optimal conditions

Derivation of pathlines

Changes of receptive fields with collinear local tendencies form a “pathline.” The shapes of pathlines can be derived as follows. First suppose, for simplicity, that the regions of fluctuation $\Omega_{\mathbf{X}_0}$ are very narrow, so they can be approximated by line segments centered on $\mathbf{X}_0$ and aligned with $\nu_i(\mathbf{X}_0)$. Let the segments be spaced such that endpoints of one segment

are exactly at the endpoints of the neighboring segments. Let $\mathscr{L}(\mathbf{X})$ be the union of segments $\Omega_{\mathbf{X}_0}$ forming a continuous curve through **X**.

Then, pathline $\mathscr{P}\mathbf{X})$ through **X** is a set of points containing all $\mathscr{L}(\mathbf{X})$ as subsets. If **X** is fixed, the slope of pathline $\mathscr{P}\mathbf{X})$ at point **X** is $\nu_i(\mathbf{X})$. When the segments are sufficiently short, it follows from the Peano existence theorem and from the theorem on continuous dependence of solutions on initial conditions and parameters (Petrovski, 1966), that the curve through **X** will be approximated by solution of this differential equation:

$$\frac{dX_2}{dX_1}=\bar{\nu}_i(\mathbf{X}). \quad (30)$$

Generally, solutions of Equation 30 are not unique. They become unique, however, when function $\bar{\nu}_i(\mathbf{X})$ is Lipschitz at X_2 in some domain $\mathscr{D}$such that

$$|\bar{\nu}_i(\mathbf{X}) - \bar{\nu}_i(\mathbf{X}')| \leq L|X_2 - X_2'|,$$

where $\mathbf{X}'=(X_1, X_2')$(Osgood's theorem; Petrovski, 1966).

For example, if $\bar{\nu}_i(\mathbf{X})$ is the expected speed of stimulation

$$\nu_e=\int_0^\infty \nu p(\nu)d\nu,$$

then pathlines $\mathscr{P}\mathbf{X}_0)$ at $\mathbf{X}_0 = (X_{1,0}, X_{2,0})$ are

$$X_2=\nu_e X_1+C_0, \quad (31)$$

for $C_0 = X_{2,0} - \nu_e X_{1,0}$.

Now suppose that regions $\Omega_{\mathbf{X}_0}$ are not confined to segments, but they constitute extended regions in (*T, S*). Then solutions of Equation 31 change from curves to bands centered on the curves. An example of such a band is illustrated using red markers in Fig. 8*A*, which corresponds to the red curve in Fig. 8*B*.

Minima of uncertainty on pathlines

On every pathline there exists a point where composite measurement uncertainty:

$$U_c(T,S)=\lambda_S S+\frac{\lambda_{\bar{S}}}{S}+\lambda_T T+\frac{\lambda_{\bar{T}}}{T}$$

(Equation 9 in the main text) is the smallest, i.e., where the following identity holds:

$$\frac{\partial U_c}{\partial S}dS+\frac{\partial U_c}{\partial T}dT=0. \quad (32)$$

After sufficiently long time (i.e., in the system's steady state), the stochastic fluctuations of tuning parameters are expected to preferentially bring cell tuning to such regions of (*T, S*) where Equation 32 is satisfied. We find such conditions by solving Equation 32 under the "pathline" constraint of Equation 31, which we rewrite as

$$S=\nu_e T+C,$$

where ν_e is the expected speed of stimulation and $C = S_0 - \nu_e T_0$ is a parameter approximately shared by a group of cells. Within each such group, cell parameters vary as if cell representations in space (T, S) moved along a pathline (or within a band of pathlines, the band defined by a small range of C). Evidently, the most likely values of S and T within such a group are

$$(T,S)=\arg\min_{T_1,S_1:S_1=\nu_e T_1+C} U_c(T_1,S_1),$$

because the likelihood that a cell has some tuning (T^*, S^*) is inversely proportional to $U_c(T^*, S^*)$. Since uncertainty function U_c is unimodal ($\lambda_S, \lambda_S, \bar{\lambda}_T, \lambda_T > 0$), on any line $S = \nu_e T + C$ there is a minimum which we find by taking into account that $\nu_e = dS/dT$:

$$\frac{\partial U_c}{\partial S}\nu_e+\frac{\partial U_c}{\partial T}=0. \quad (33)$$

Solving Equation 33 for S and T yields

$$S=\sqrt{\frac{\nu_e\lambda_{\bar{S}}T^2}{(\lambda_S\nu_e+\lambda_T)T^2-\lambda_{\bar{T}}}}. \quad (34)$$

Equation 34 describes a set of conditions in (T, S) that has a hyperbolic shape in both linear and logarithmic coordinates. Equation 34 is identical to the equation that describes the optimal conditions of motion measurement in Gepshtein et al. (2007).

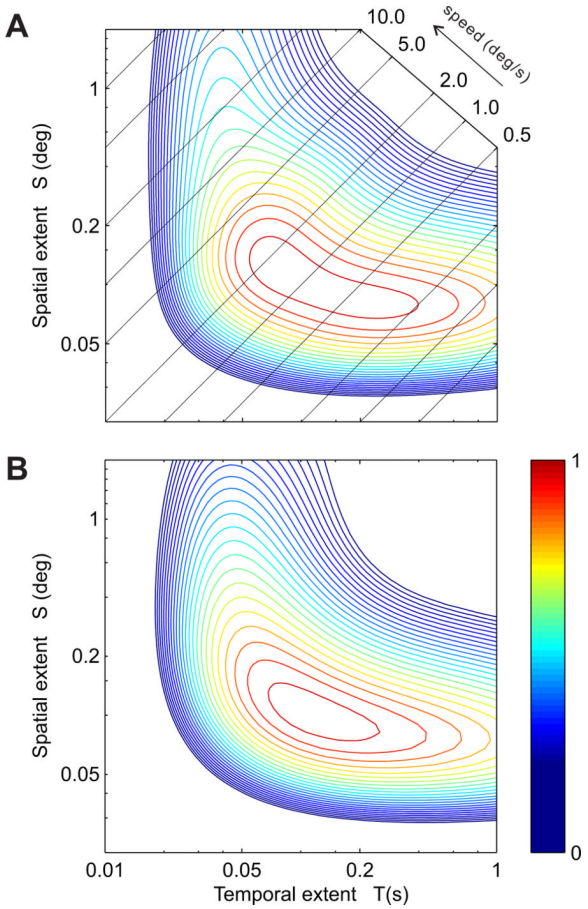

Figure 1. Visual contrast sensitivity in a space-time graph

(*A*) Human spatiotemporal contrast sensitivity (*Kelly function*) transformed from the frequency domain to space-time (Kelly, 1979; Nakayama, 1985; Gepshtein et al., 2007). The axes are the temporal and spatial extents of receptive fields. The colored contours (*isosensitivity contours*) represent contrast sensitivity. The oblique lines represent speeds (*constant-speed lines*). The lines are parallel to one another in logarithmic coordinates. (*B*) Spatiotemporal sensitivity function that emerges in the present simulations from independent stochastic fluctuations of receptive fields in multiple motion-sensitive neurons.

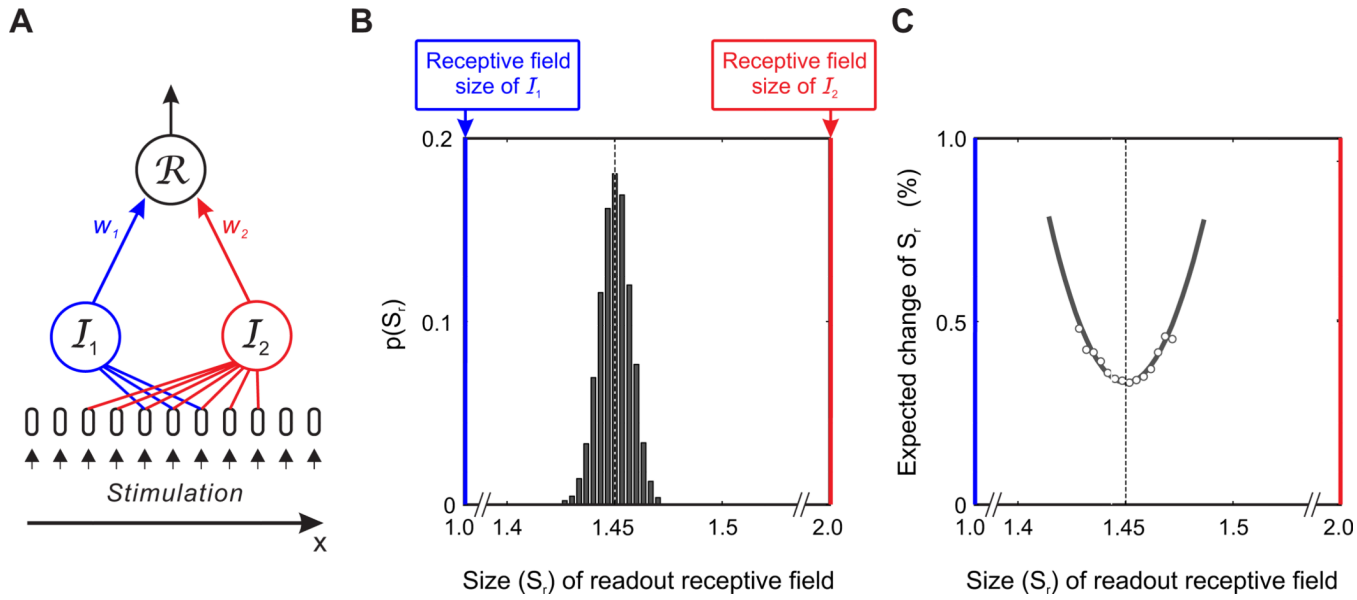

Figure 2. Mechanism and dynamics of receptive field size

(*A*) Basic neural circuit. Input cells $\mathcal{I}_1$ and $\mathcal{I}_2$ receive stimulation from sensory surface *x*, indicated by the converging lines in corresponding colors. The range of inputs for each cell is its receptive field. $\mathcal{R}$ is the readout cell whose activation is mediated by input-readout weights w_1 and w_2. The weights are dynamic: they depend on coincidence of activation of input and readout cells (Equation 7 and Fig. 3A). The weights determine the size of the readout receptive field. (*B*) Central tendency of readout receptive field (S_r in Equation 15), measured in numerical simulations of the circuit in A. As the input-readout weights are updated, S_r fluctuates on the interval between the smallest and largest input receptive field sizes, marked on the two sides of the plot. The histogram represents probabilities of the different magnitudes of S_r over the course of numerical simulation (Appendix A). The dashed line is the central tendency of S_r: the most likely receptive field size. (*C*) Variability of S_r. The data points represent average *changes* of S_r for different magnitudes of S_r. The more S_r is removed from its central tendency (the dashed line copied from B) the larger is its variation, akin to the variation of uncertainty of measurement by a single receptive field captured by Equation 2.

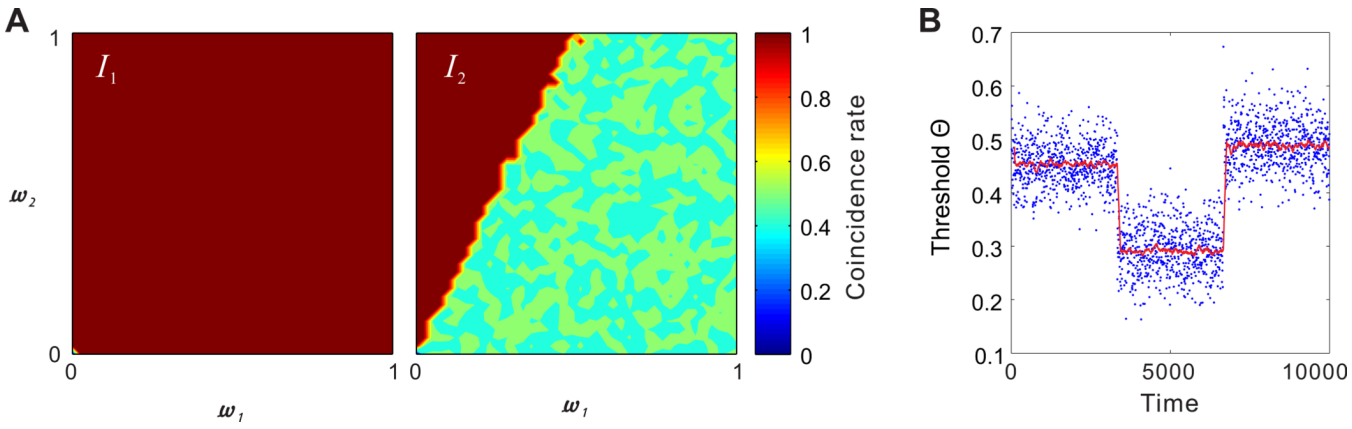

Figure 3. Coincident firing of input and readout cells in the basic circuit

(*A*) Coincidence rate c_i of spiking for input and readout cells (Equation 14) for all combinations of input-readout weights w_1 and w_2, plotted separately for cells $\mathcal{I}_1$ (left) and $\mathcal{I}_2$ (right). For $\mathcal{I}_1$, all input spikes are accompanied by readout spikes, so that $c_1 = 1$ for every combination of w_1 and w_2. For $\mathcal{I}_2$, input spikes sometimes do not lead to firing of the readout cell. Since $\mathcal{I}_1$ is more likely to fire together with the readout cell than $\mathcal{I}_2$, weight w_1 is on average larger than weight w_2, and the size of readout receptive field gravitates toward the size of receptive field in $\mathcal{I}_1$ which is smaller than the size of receptive field in $\mathcal{I}_2$. (*B*) Adaptive response threshold Θ of readout cell for three regimes of measurement. The blue dots represent the values of Θ recorded in 10,000 iterations (every fifth value is shown). The simulation was divided to three periods of equal length, each using a different computation of input cell responses, from left to right: Equation 4, Equation 9, and Equation 8. Threshold Θ fluctuates in the vicinity of a value that is distinct for each method of response computation; it is represented by the red line: the running average of 100 previous magnitudes of Θ.

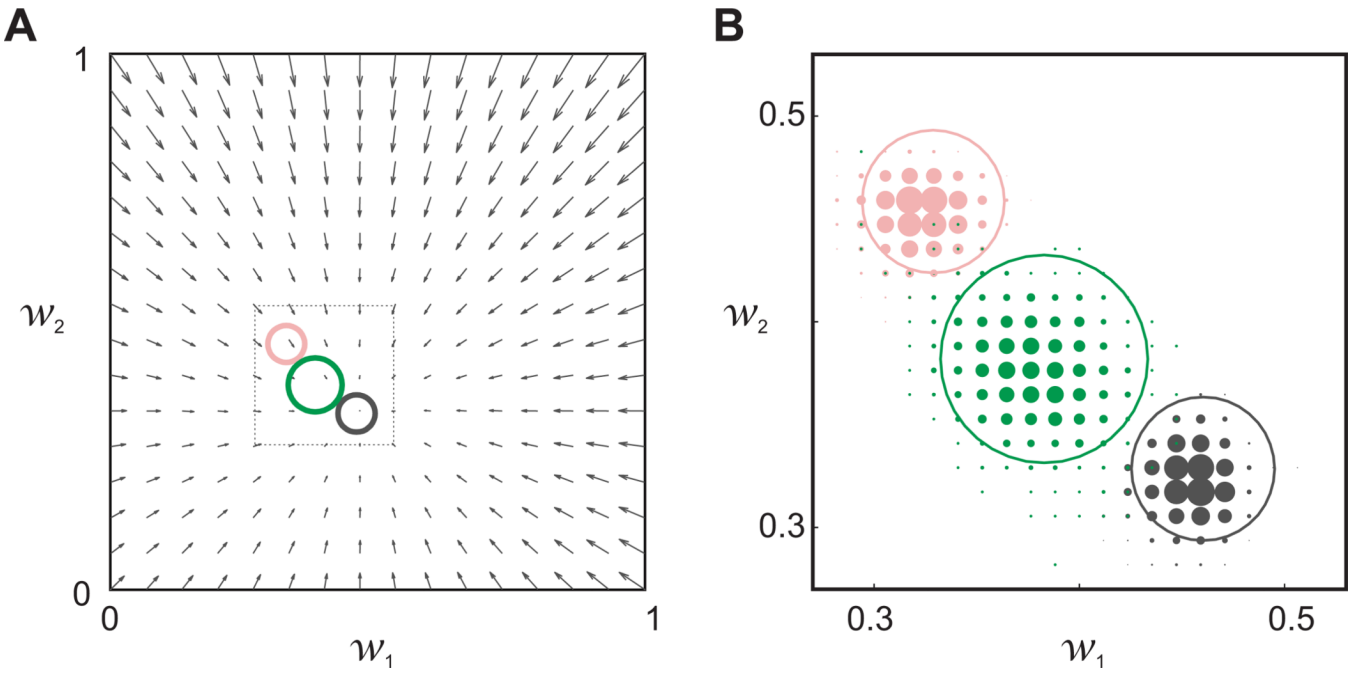

Figure 4. Stable-state behavior of the basic circuit

(*A*) Circuit dynamics led to remarkably stable outcomes, illustrated here in the space of input-readout weights w_1 and w_2. The plot summarizes the results of multiple numerical simulations with different starting pairs of weights (w_1, w_2). Each arrow represents the mean direction and magnitude of weight change measured at the arrow origin. The region to which the weights tended to converge is marked by a gray outline, magnified in panel *B*. (The two other outlines, in pink and green, are explained in panel *B*.) (*B*) Enlargement of a region of the weight space in panel *A*. The gray outline marks the same region in (w_1, w_2) as the gray outline in panel *A*. The outline is superimposed on a histogram of weights: a grid of (gray) disks of which the sizes represent how often the simulation yielded the pairs of weights (w_1, w_2) at corresponding disk locations. When circuit activity was controlled by stimulus location only, weight w_1 tended to be larger than weight w_2, and so the size of the readout receptive field tended toward the size of smaller input receptive field, as reported in Fig. 2*B*–*C*. When circuit activity was controlled only by stimulus frequency content, the weights reversed: w_2 tended to exceed w_1, and so the size of the readout receptive field tended toward the size of the larger input receptive field (cell $\mathcal{I}_2$), summarized by the histogram in pink. When circuit activity was controlled by both stimulus location and frequency content, the weights had intermediate values, summarized by the histogram in green, yielding readout receptive fields of intermediate size.

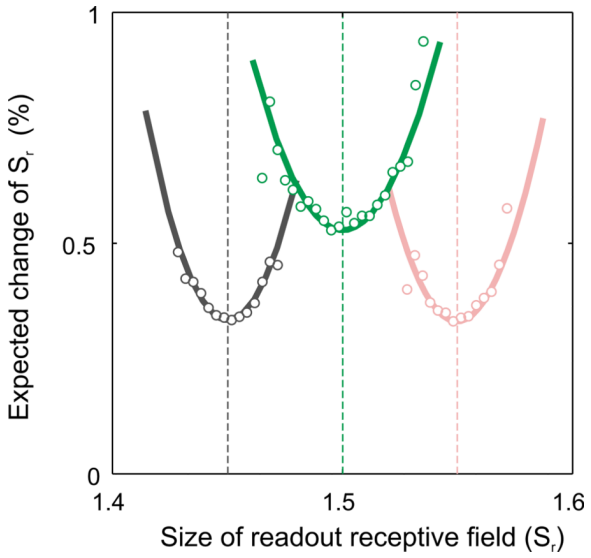

Figure 5. Lawful fluctuations of receptive field size

Variability of readout receptive field size (S_r) for different regimes of measurement: measurement of stimulus location alone (gray), stimulus frequency content alone (pink), and jointly stimulus location and frequency content (green). The data points represent average changes of S_r for different magnitudes of S_r (as in Fig. 2*C*). In all cases, the more S_r was removed from its central tendency (the dashed line) the larger was its variation.

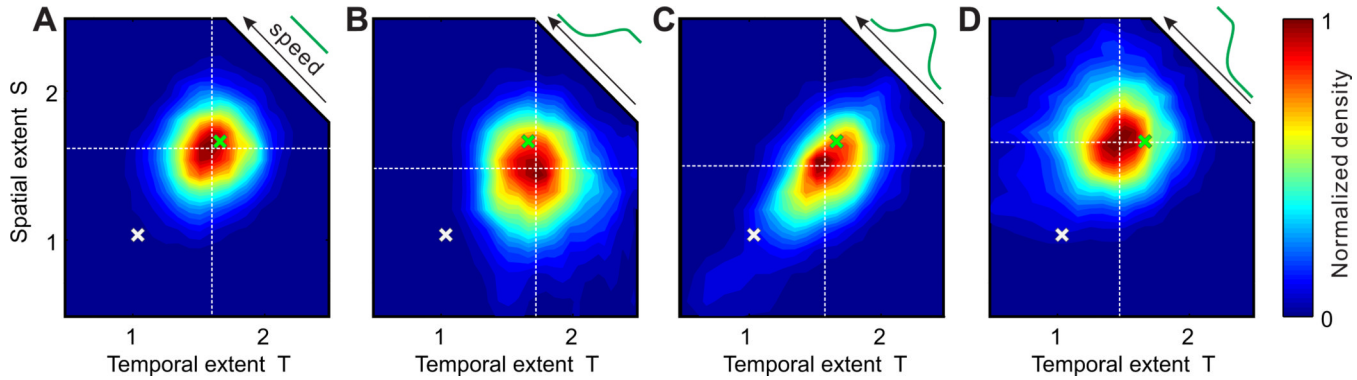

Figure 6. Stochastic tuning of readout receptive fields in space-time

The coordinates in every panel represent the temporal and spatial extents, *T* and *S*, of a receptive field. (*A*) Preferred size of readout receptive field. The white cross indicates the starting receptive field size $\mathbf{X}_0 = (T_0, S_0)$. The green cross indicates a neutral point, at which the weights of all the input cells to the readout cell are equal to one another. (The white and green crosses have the same locations in all panels.) The map in the background is the probability of the different sizes of readout receptive fields over the course of simulation (10,000 iterations), indicating that the size of readout receptive field tends to drift toward a certain spatial-temporal size ("preferred size") marked by the intersection of white dotted lines at $\mathbf{X}_r^* = (T_r^*, S_r^*)$. (*B–D*) Effect of the prevailing speed of stimulation on the readout receptive field. Simulations were performed as for panel A, but using biased stimulus distributions, characterized by different prevailing speeds v_e (Equation 24) represented by the stimulus probability distributions plotted in green at top-right of each panel (0.2 deg/s in B, 1.0 deg/s in C, and 5.0 deg/s in D).

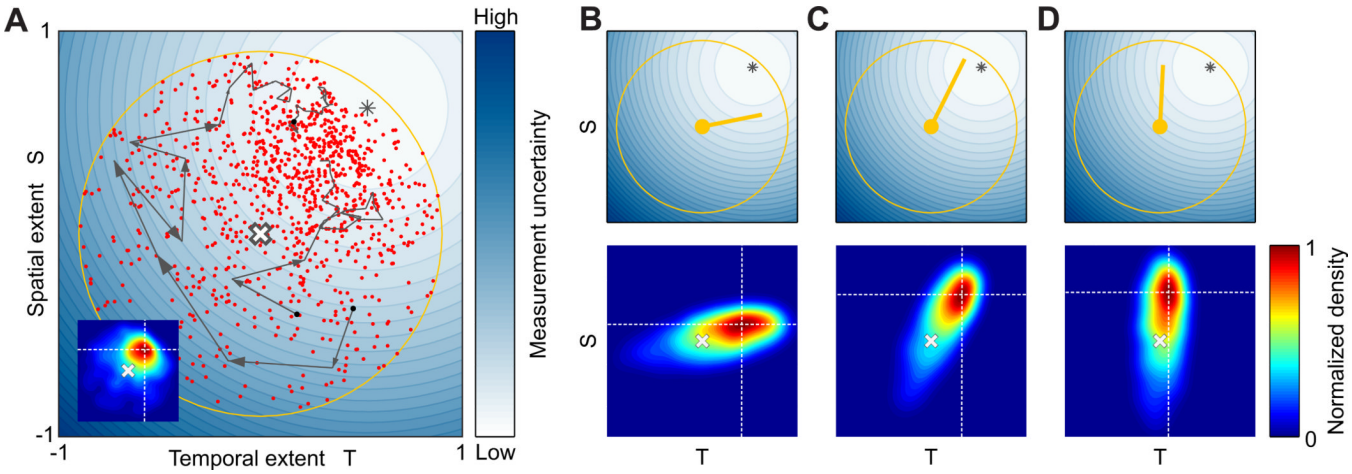

Figure 7. Consequences of stochastic tuning for single receptive fields

Coordinates of every panel represent the temporal and spatial extents of receptive fields relative to the center of the region of interest marked by the white cross. (*A*) Effect of measurement uncertainty. Initially all receptive fields (N = 1, 000) have the same parameters $\mathbf{X}_0 = (\mathbf{T}_0, \mathbf{S}_0)$ marked by the white cross (at the same location in all panels). Red dots represent the final sizes of receptive fields ("end points"), each after 700 iterations by Equation 11. The large yellow circumference contains the region of permitted fluctuations (Equation 12). The contour plot in the background represents the measurement uncertainty function (Equation 3) whose minimum is marked by the gray asterisk. The three trajectories composed by gray arrows illustrate 20 updates of three model neurons (arbitrarily selected for this illustration). The lengths of arrows are proportional to measurement uncertainties at arrow origins, and arrow directions are sampled from an isotropic probability distribution (**R** in Equation 11). The inset is a normalized histogram of all end points, indicating that receptive field sizes tend to drift toward lower measurement uncertainty. (*B–D*) Effect of stimulation. Results of simulations of stochastic tuning performed as in *A*, but at three different prevailing speeds of stimulation (Equation 24). The three columns show results for different prevailing speeds, increasing from *B* to *D*. The direction of receptive field drift depends on the prevailing stimulus speed, indicated by the directed yellow markers in top plots, and by the high concentration of end points in the histograms in bottom plots. Intersections of the white grid lines in bottom panels mark *preferred locations* of receptive fields, as in Fig. 6. In the yellow directed markers (also used in Fig. 8*A*), the initial location of receptive fields is represented by a small disk and the direction of receptive field drift is represented by a line to the mean end point of receptive field fluctuations.

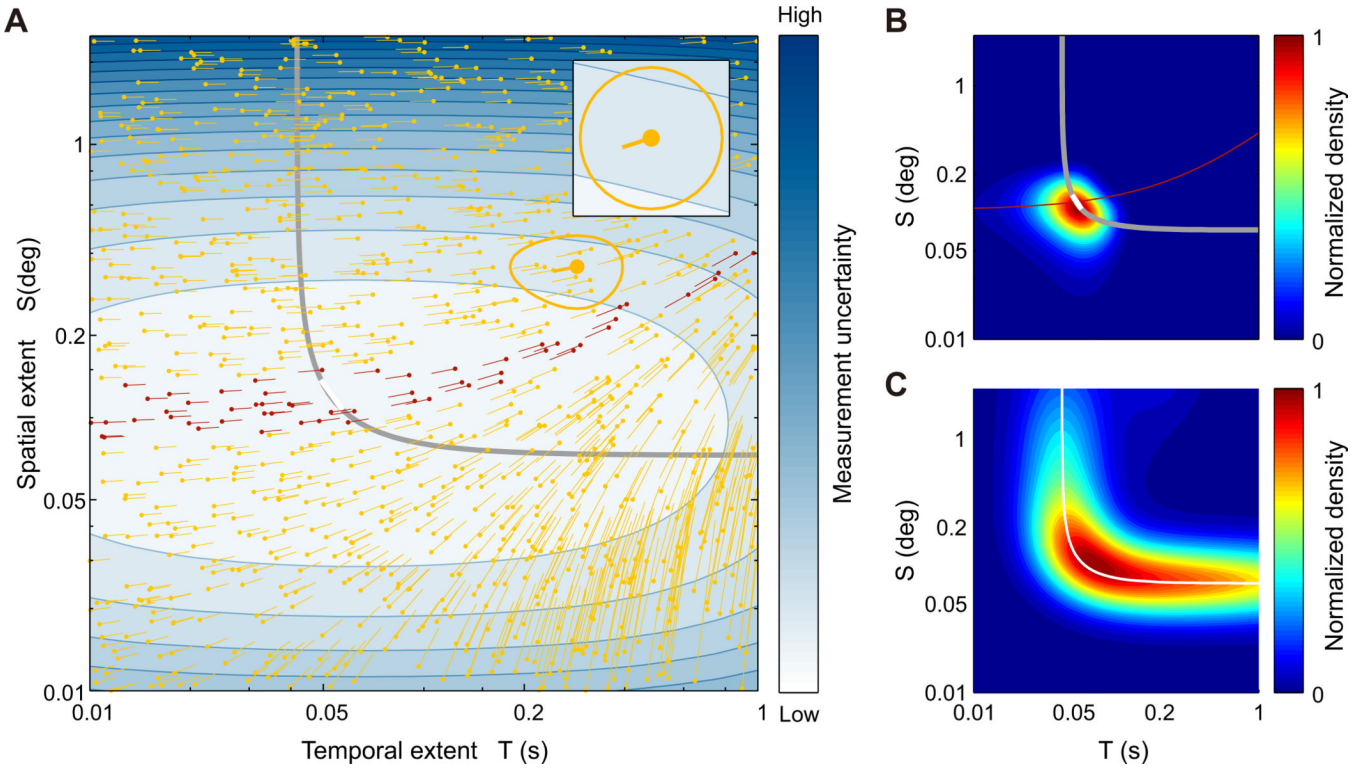

Figure 8. Stochastic tuning of motion-sensitive cells across parameter space (*T, S*)

Parameters *T* and *S* correspond to the temporal and spatial extents of receptive fields. (*A*) Local tendencies of receptive field fluctuations. The small directed markers represent mean directions of receptive field fluctuation (Fig. 7). The inset on top right contains one such marker magnified in linear coordinates, as in Fig. 7*B–D*. (The shape of local boundary Ω is different in the inset and in the main figure because of the logarithmic coordinates in latter.) The markers in red represent a set of adjacent *pathlines* (see text). Measurement uncertainty is displayed in the background as a contour plot. The gray curve represents optimal conditions (“optimal set") of speed measurement derived as in Gepshtein et al. (2007). The directed markers across point to the optimal set. If not for conservation of receptive field size (Equation 12), the local tendencies from the locations in red would converge on the white segment of the optimal set. (*B–C*) Results of stochastic tuning. The heat maps are normalized histograms of end-point densities of receptive field tuning. In *B*, the histogram is computed for the conditions highlighted in red in panel *A*. In *C*, the histogram is computed for the entire parameter space. (The focus of high density and the white segment in panel *B* are slightly misaligned because of an asymmetry of cell distribution within the group of highlighted pathlines.)

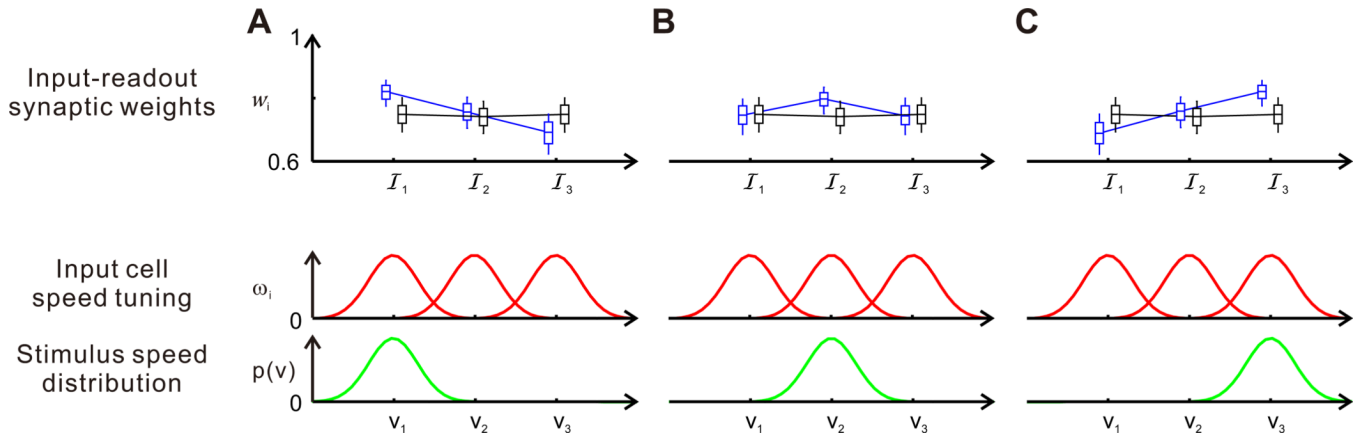

Figure 9. Illustration of stimulus bias in the basic circuit

Panels *A–C* illustrate outcomes of simulations of the basic circuit using three different distributions of stimulus speed. The stimulus distributions are represented by green curves in the bottom panels, with the mean stimulus speed increasing from *A* to *C*. Middle panels (ω_i) illustrate tuning functions (in red) for three input cells centered on tuning speeds v_i, $i \in \{1, 2, 3\}$. In the top panels, the blue boxplots represent input-readout weights w_i from over 5, 000 iterations, using stimuli sampled from the speed distributions in the corresponding bottom panels. The top panels also contain plots (in black) of input-readout weights observed for stimuli sampled from a uniform distribution of speed (the same for all top panels). (In the boxplots, the boxes mark the 25th and 75th percentiles, and the whiskers mark the 10th and 90th percentiles, of the distribution of weights.)

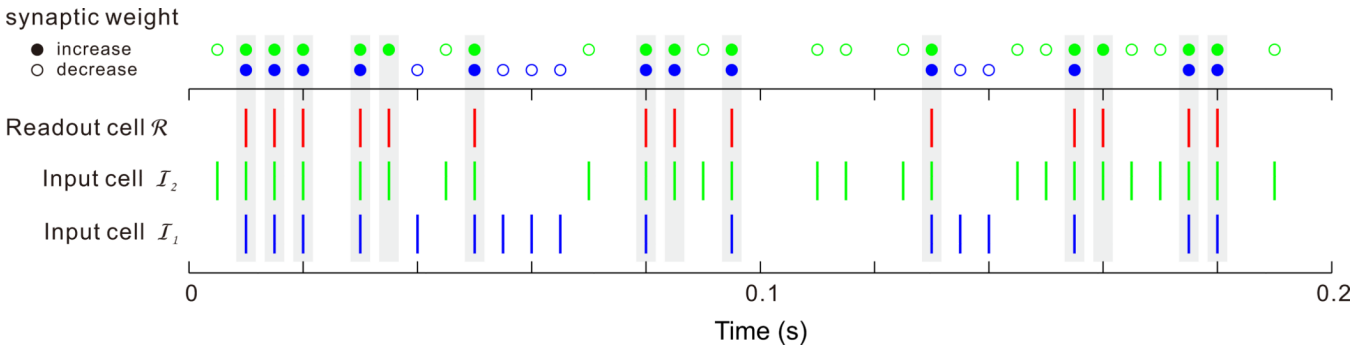

Figure 10. Illustration of simulated spiking activity in input and readout cells

Input responses were modeled using a homogeneous Poisson spike generator. Blue and green marks indicate the timing of spikes in input cells $\mathcal{I}_1$ and $\mathcal{I}_2$ within 200 ms after stimulus presentation. In this illustration, the normalized response rates of input cells are $r_1 = 0.6$ and $r_2 = 0.9$ and the maximal firing rate r_{max} is 200. Red bars mark the timing of readout cell spikes. The gray regions enclose input spikes coincident with readout spikes. Since cell $\mathcal{I}_2$ tended to respond when cell $\mathcal{I}_1$ responded, thus activating the readout cell, many spikes of cell $\mathcal{I}_1$ were followed by readout spikes, but spikes of cell $\mathcal{I}_2$ often elicited no readout spikes. The effect of spike coincidence on input-readout weights is represented by the circles in top two rows. The filled and unfilled circles stand, respectively, for increments and decrements of weight. Coincidence rates (Equation 14) for this illustration are $c_1 = 12/18 = 0.67$ and $c_2 = 14/26 = 0.54$.

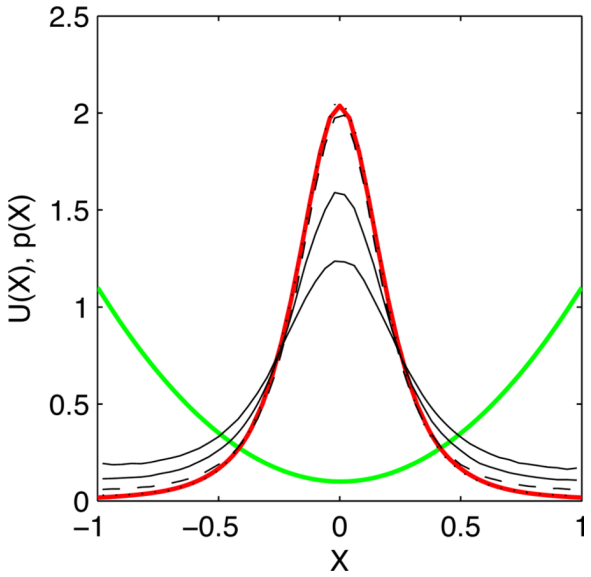

Figure 11. Steady-state parameter distributions

The red line is a prediction of receptive field parameter distribution (Equation 22) in a system with receptive field fluctuations constrained by a reflective boundary. **X** stands for receptive field size, here normalized to interval [−1 1]. The uncertainty function $U(\mathbf{X})$ is represented by the green curve. The four black curves are results of computational experiments with different fluctuation rates γ. The curves are histograms of parameter distributions, $p(\mathbf{X})$, each after 1, 000 iterations.